Lyman Continuum Escape Fraction from Low-mass Starbursts at $z = 1.3$[*]

Anahita Alavi[1] , James Colbert[1] , Harry I. Teplitz[1] , Brian Siana[2] , Claudia Scarlata[3] , Michael Rutkowski[4] ,
Vihang Mehta[3] , Alaina Henry[5] , Y. Sophia Dai (戴昱)[6] , Francesco Haardt[7] , and Micaela Bagley[8]

[1] IPAC, California Institute of Technology, 1200 E. California Boulevard, Pasadena, CA 91125, USA; anahita@ipac.caltech.edu
[2] Department of Physics and Astronomy, University of California, Riverside, CA 92521, USA
[3] Minnesota Institute for Astrophysics, University of Minnesota, Minneapolis, MN 55455, USA
[4] Department of Physics and Astronomy, Minnesota State University, Mankato, MN 56001, USA
[5] Space Telescope Science Institute, 3700 San Martin Drive, Baltimore, MD 21218, USA
[6] Chinese Academy of Sciences South America Center for Astronomy (CASSACA)/National Astronomical Observatories of China (NAOC), 20A Datun Road,
Beijing 100012, People's Republic of China
[7] DiSAT, Universiá degli Studi dell'Insubria, I-22100 Como, Italy
[8] Department of Astronomy, The University of Texas at Austin, Austin, TX 78712, USA

Abstract

We present a new constraint on the Lyman continuum (LyC) escape fraction at $z \sim 1.3$. We obtain deep, high sensitivity far-UV imaging with the Advanced Camera for Surveys Solar Blind Channel on the Hubble Space Telescope, targeting 11 star-forming galaxies at $1.2 < z < 1.4$. The galaxies are selected from the 3D-HST survey to have high Hα equivalent width (EW) with an EW > 190 Å, low stellar mass ($M_* < 10^{10} M_\odot$), and U-band magnitude of $U < 24.2$. These criteria identify young, low metallicity star-bursting populations similar to the early star-forming galaxies believed to have reionized the universe. We do not detect any LyC signal (with a signal-to-noise ratio > 3) in the individual galaxies or in the stack in the far-UV images. We place 3σ limits on the relative escape fraction of individual galaxies to be $f_{\rm esc,rel} < [0.10\text{–}0.22]$ and a stacked 3σ limit of $f_{\rm esc,rel} < 0.07$. Measuring various galaxy properties, including stellar mass, dust attenuation, and star formation rate, we show that our measured values fall within the broad range of values covered by the confirmed LyC emitters from the literature. In particular, we compare the distribution of Hα and [O III] EWs of confirmed LyC emitters and non-detections, including the galaxies in this study. Finally, we discuss if a dichotomy seen in the distribution of Hα EWs can perhaps distinguish the LyC emitters from the non-detections.

Unified Astronomy Thesaurus concepts: Galaxy evolution (594); Reionization (1383); Starburst galaxies (1570); Ultraviolet astronomy (1736); Intergalactic medium (813); Emission line galaxies (459); High-redshift galaxies (734)

1. Introduction

Reionization is the last major phase transition in the universe, when Lyman continuum (LyC) photons ionized the intergalactic medium (IGM). Hundreds of hours of observations by the leading facilities in the world have been devoted to understanding when and how reionization happened. From observations studying the duration of reionization, it is now believed that the reionization era ended by redshift ∼6. This has been demonstrated by various methods, including the Gunn–Peterson effect in the spectra of high-redshift QSOs (e.g., Fan et al. 2006) and the downturn seen in the fraction of Lyα emitters among Lyman break galaxies beyond $z = 6$ (e.g., Stark et al. 2010; Pentericci et al. 2014; Mason et al. 2019). In addition, the Planck Collaboration et al. (2016) estimate an average redshift between 7.8 and 8.8 for this epoch, adopting an instantaneous reionization model.

However, despite a considerable number of studies, it remains uncertain which sources dominated the emission of LyC photons during the reionization epoch. Both active galactic nuclei (AGNs) and young massive stars produce LyC photons and can contribute to the reionization of the IGM. Though, there are some studies indicating that AGNs might be

important (Giallongo et al. 2015, 2019), many studies have concluded that they cannot be the primary contributors to reionization (e.g., Willott et al. 2005; Siana et al. 2008; Masters et al. 2012; Matsuoka et al. 2018; Parsa et al. 2018; Kulkarni et al. 2019).

In the absence of AGNs, the young massive stars in star-forming galaxies seem to be the primary sources of LyC photons in the early universe. Recent studies (e.g., Bouwens et al. 2017; Livermore et al. 2017; Atek et al. 2018; Ishigaki et al. 2018; Ono et al. 2018; Pelló et al. 2018; Yue et al. 2018) of UV luminosity functions at $z > 6$ have found steep faint-end slopes suggesting a large number density of faint star-forming galaxies at these redshifts. These findings suggest that faint star-forming galaxies may play a significant role during the reionization era (e.g., Robertson et al. 2013, 2015; Bouwens et al. 2015; Mason et al. 2015). In particular, (1) faint galaxies must produce sufficient LyC photons and (2) these photons must escape absorption within interstellar medium (ISM) and reach the IGM. The former point can be expected as the faint star-forming galaxies are the most abundant galaxies particularly in the early universe. However, the ionizing photon production rate of these faint galaxies still requires investigation (Emami et al. 2020). To quantify point number (2) mentioned above, we need to measure the fraction of LyC photons that escape (i.e., $f_{\rm esc}$) the ISM and reach the IGM.

A direct measure of $f_{\rm esc}$ at $z > 4$ is difficult due to the high opacity of IGM (Inoue et al. 2014). Therefore, direct study of

escaping LyC photons is limited to low and intermediate redshifts. Early studies of the LyC emission escaping nearby galaxies (Leitherer et al. 1995; Deharveng et al. 2001; Grimes et al. 2009) resulted only in upper limits, suggesting an f_{esc} of a few percent. At higher redshifts ($z \sim 3$), early studies (Shapley et al. 2006; Nestor et al. 2011) reported detections, but several of those detections turned out to be contaminated by foreground sources at lower redshifts (Vanzella et al. 2010, 2012; Siana et al. 2015). Later, more studies found low redshift contaminants in their samples of LyC emitter candidates (Vanzella et al. 2012; Mostardi et al. 2015; Grazian et al. 2016). Additional high-z studies found null detections and only obtained upper limits (Siana et al. 2007, 2010; Iwata et al. 2009; Boutsia et al. 2011; Rutkowski et al. 2016, 2017; Smith et al. 2018).

Recently, several LyC galaxies have been detected at low ($z = <0.4$; Leitet et al. 2013; Borthakur et al. 2014; Leitherer et al. 2016; Izotov et al. 2016a, 2016b, 2018a, 2018c) and high redshifts ($z = 2–4$; Shapley et al. 2016; Vanzella et al. 2016, 2018; Bian et al. 2017; Naidu et al. 2017; Steidel et al. 2018; Fletcher et al. 2019; Rivera-Thorsen et al. 2019). There is also a very recent study by Saha et al. (2020) who found an LyC emitter at $z = 1.42$. However, all of the other attempts at intermediate redshifts of $z \sim 1$ have given null results (Malkan et al. 2003; Siana et al. 2007, 2010; Cowie et al. 2009; Bridge et al. 2010; Rutkowski et al. 2016). Although the rate of success in finding LyC emitters at all redshifts has been low, some detections at $z \sim 1$ should have been expected. In fact, there are two reasons that one might expect the detection of LyC emission at $z \sim 1$ to be easier than at higher redshifts: (1) there is a loss of signal due to the increasing luminosity distance at $z > 2$ relative to $z \sim 1$ and (2) the average opacity of the line of sight (LOS) through the IGM increases with redshift.

The recent detections of LyC emission have been accomplished with the combination of high sensitivity observations and apparently effective selection techniques. One such technique identifies galaxies with high ratios of [O III]/[O II], which is potentially associated with density-bounded H II regions. Nakajima & Ouchi (2014) presented a photoionization model calculation with CLOUDY (Ferland et al. 1998) that suggests that galaxies with high [O III]/[O II] ratios are good candidate high f_{esc} objects. They also showed that their finding is consistent with the ratio of [O III]/[O II] $\sim$1–4 of two LyC leakers (Leitet et al. 2011, 2013) known at that time. The potential of this criterion to identify LyC leakers was later investigated in several low-redshift studies of galaxies with [O III]/[O II] $\gtrsim$5 (Izotov et al. 2016a, 2016b, 2018a, 2018c), which were successful in finding LyC emitters using the Cosmic Origins Spectrograph (COS) on the Hubble Space Telescope (HST). At high redshift, the first LyC emitter that was discovered, *Ion*2, was found to have a high ratio of [O III]/[O II] $\gtrsim$10 (Vanzella et al. 2016). In addition, Faisst (2016) found a positive correlation between the [O III]/[O II] ratio and f_{esc} compiling 13 detections and upper limits from the literature. In contrast, Stasińska et al. (2015) argued that this line ratio on its own is not a sufficient diagnostic tool for LyC leakage. This was later validated by several unsuccessful searches of LyC leakage among galaxies with high [O III]/[O II] ratios (Rutkowski et al. 2017; Naidu et al. 2018) and a statistical analysis by Izotov et al. (2020).

Relatedly, many of the confirmed LyC emitters at high (Vanzella et al. 2016; Naidu et al. 2017; Fletcher et al. 2019) and low redshifts (Izotov et al. 2016a, 2016b, 2018a, 2018c) also display extreme [O III] EWs. Indeed, extreme [O III] emitters at $z = 0.1 - 0.3$, known as "green pea" galaxies (Cardamone et al. 2009), have long been studied as potential candidates for high LyC escape fraction (Jaskot & Oey 2013; Nakajima & Ouchi 2014; Henry et al. 2015; Izotov et al. 2016a, 2016b, 2018a, 2018c). However, recently, Naidu et al. (2018) found no LyC detection for their sample with high [O III] EWs, thus raising a question about the reliability of extreme [O III] EW as an effective tracer of LyC emission. Similar conclusions are also found for individual non-detections at low redshifts by Izotov et al. (2017) and high redshifts by Amorín et al. (2014) and Vasei et al. (2016).

In this paper, we search for LyC photons in low-mass emission-line galaxies during a burst in their star formation. We select galaxies to have strong Hα emission lines with rest-frame EW > 190 Å. The Hα line is an indicator of an instantaneous star formation rate (SFR), and thus it traces young and hot O-type stars, which are responsible for the LyC production in galaxies. To this end, we conduct a deep far-UV imaging program and exploit the high sensitivity and high spatial resolution of the Solar Blind Channel (SBC) of the Advanced Camera for Surveys (ACS) (Ford et al. 1998) onboard HST. Our observations would be sensitive to LyC photons at $z \sim 1.3$, a redshift from which there has been only one very recent detection of escaping ionizing radiation (Saha et al. 2020) and all of the other efforts have yielded null results.

This paper is organized as follows. Section 2 presents the HST observations, reduction of the data and sample selection. In Section 3, we discuss the steps involved in measuring the observed far-UV photometry. In Section 4, we show the results including upper limits to the LyC fluxes of individual galaxies and stacks, and we calculate the upper limit of the escape fraction of ionizing photons. Section 5 compares our study and other LyC efforts in the literature to better understand the galaxy properties that favor LyC leakage.

Throughout the text, we use a flat Lambda cold dark matter cosmology with $H_0 = 70$ km s^{-1} Mpc^{-1}, $\Omega_M = 0.3$, and $\Omega_\Lambda = 0.7$. All magnitudes are in the AB system (Oke & Gunn 1983).

2. Observation and Data Reduction

2.1. Sample Selection

We targeted 11 star-forming galaxies detected by the 3D-HST survey (PI: P. van Dokkum; Brammer et al. 2012; Momcheva et al. 2016) of the Great Observatories Origins Deep Survey-South (GOODS-South) and Cosmological Evolution Survey (COSMOS) fields with spectroscopic redshifts between $1.2 < z < 1.4$. The lower end of the redshift range is selected to avoid contamination from non-ionizing UV photons redward of the Lyman limit at 912 Å and the upper end ensures high sensitivity to LyC photons (see Figure 1).

To select targets from the 3D-HST spectra, we used custom measurements (Rutkowski et al. 2016), using the code originally developed for the WFC3 IR Spectroscopic Parallel survey (WISP; PI: M. Malkan; Atek et al. 2010). Galaxies are selected to have strong Hα emission lines with a rest-frame EW > 190 Å and low stellar masses of log($M_*/M_\odot$) < 10. These low stellar masses suggest low metallicities in our
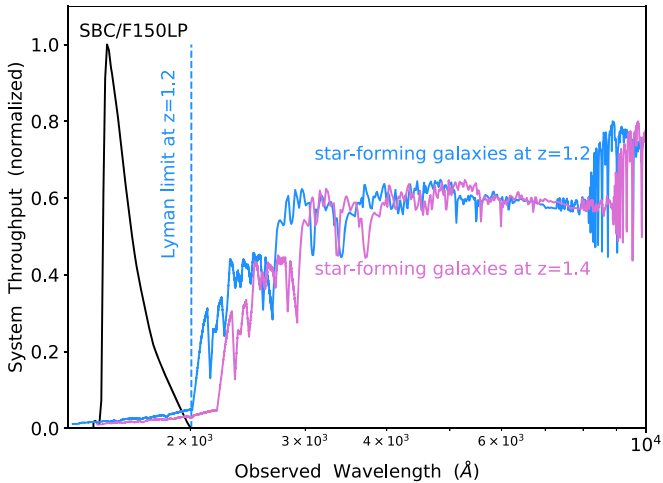
Figure 1. Total system throughput for the ACS SBC/F150LP filter. Two model spectral energy distributions (SEDs) of star-forming galaxies at $z = 1.2$ (solid blue) and 1.4 (solid purple); the low and high cuts of our redshift range are also shown to demonstrate that no non-ionizing flux enters this system throughput. The SEDs are from BC03 synthetic stellar population models (Bruzual & Charlot 2003) representing normal star-forming galaxies at $z \sim 1$ with a constant SFR, solar metallicity, an age of 100 Myr, and $E(B − V) = 0.1$. The dashed blue line shows the Lyman limit cut at rest frame 912 Å at $z = 1.2$.
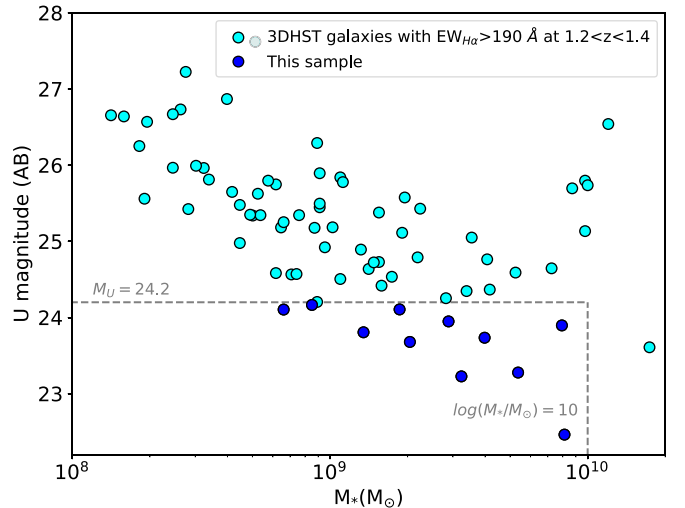

Figure 2. The U-band magnitude versus stellar mass for all of the galaxies with $1.2 < z < 1.4$ and EW(Hα) > 190 Å in the 3D-HST catalogs. The dashed lines show our U-band magnitude and stellar mass cuts at $U = 24.2$ and $\log(M_*/M_\odot) < 10$, respectively. Our final sample consists of 11 sources, which happened to be located in the COSMOS and GOODS-South fields specified as blue circles.

sample (e.g., Wuyts et al. 2012; Sanders et al. 2015). Therefore, our sample includes young, low metallicity, and low-mass starbursting populations, similar to the class of galaxies believed to have reionized the universe. We note that the lower mass selection criterion only excludes two galaxies from our sample as the extreme emission-line selected galaxies (i.e., high EW) have preferentially low stellar continuum and hence low stellar masses. We further require that these galaxies are bright enough that they can provide a meaningful limit to LyC escape fraction, with U-band <24.2 in the Canada-France-Hawaii Telescope (CFHT) MegaCam U-band (Erben et al. 2009; Hildebrandt et al. 2009) or the Very Large Telescope (VLT) Visible Multi Object Spectrograph (VIMOS) U-band (Nonino et al. 2009) images. As a result of this criterion, the selected galaxies have UV luminosities similar to $L^*_{\rm UV}$ at $z = 1.3$ (using the $L^*_{\rm UV}$ estimate from Alavi et al. 2016). Figure 2 summarizes our selection criteria. We plot all of the high Hα EW galaxies within 3D-HST, and show the UV magnitude and stellar mass cut that selects appropriate targets. A list of targets is given in Table 1.

2.2. Observations

The goal of this work is to search for escaping LyC photons from strong emission-line galaxies at $1.2 < z < 1.4$. To this end, we obtained far-UV imaging (program ID 14123, PI: J. Colbert) of our targets using the F150LP filter of SBC on ACS (Ford et al. 1998). This filter has significant transmission in the wavelength range of $1450 < \lambda < 2000$ Å (see Figure 1). The blue cutoff avoids the contamination from the geocoronal emission lines (Lyα and O I lines at 1304 and 1356 Å), which would significantly increase the background in the images. The red cutoff is dictated by the decreasing sensitivity of the Multi-Anode Microchannel Array (MAMA) toward redder wavelengths (Siana et al. 2010). The effective wavelength of this filter is $\lambda_{\rm eff} = 1616.67$ Å, which probes LyC photons at $\lambda_{\rm rest} \sim 700$ Å at $z = 1.3$. We note that most LyC searches

including spectroscopic (COS observations of local LyC emitters in Izotov et al. 2016a, 2016b, 2018a, 2018c) and photometric studies (WFC3/UVIS observations of high-redshift LyC emitters in Vanzella et al. 2016; Naidu et al. 2017; Fletcher et al. 2019), are sensitive to LyC flux at 900 Å. The neutral hydrogen opacity at $\lambda_{\rm rest} \sim 900$ Å is about twice that at $\lambda_{\rm rest} \sim 700$ Å, because the photoionization cross section decreases as ν^{-3}. In addition, the shape of ionizing spectrum should also be taken into account when we compare the LyC fluxes at 700 and 900 Å wavelengths. However, the relative difference in intrinsic LyC emission at these two wavelengths is less significant than the factor of 2 caused by the hydrogen opacity (Steidel et al. 2016; Chisholm et al. 2019).

The MAMA detector of SBC is a photon-counting device and is not affected by cosmic rays. The detector has no read noise and its primary source of noise is dark current. The SBC dark current has two components. The first is a steady, spatially uniform count rate that does not change with the detector temperature. It is estimated to be a very stable value of 8.11×10^{-6} cts pix s^{-1} (Avila 2017). The second component is a temperature-dependent glow that rises at $T > 25°$C. In previous studies (Teplitz et al. 2006; Siana et al. 2007; Avila 2017), it has been noted that the variable dark glow is most prominent near the center of the chip and the lower left corner of the detector has a stable dark rate even at elevated temperatures. Therefore, we designed our observations to place all of our targets in the detector corner least affected by the central glow (position $x = 250$, $y = 250$ pixel on the SBC detector), similar to the strategy of Siana et al. (2010).

Each target is imaged in one visit to a varying depth of one, two, or three orbits depending on the galaxy's rest-UV brightness (also see Section 4.3). Each orbit consists of four dithered exposures with similar exposure times of 654 or 692 s.

2.3. Data Reduction

We downloaded the raw data from the Barbara A. Mikulski Archive for Space Telescopes (MAST), which we then processed using the PYRAF/STSDAS CALACS program to

Table 1
SBC Sample

ID	R.A. (deg)	Decl. (deg)	z	EW$_{rest}$ ($H\alpha$)[Å]	EW$_{rest}$([O III])[Å]	log($M_*/M_\odot$)[a]	A_v[a]	log(SFR)[$M_\odot$ yr^{-1}] [a]
cosmos-1-111	150.07448	2.4172121	1.254	193.0	…[b]	9.31	0.4	−0.30
cosmos-3-69	150.09259	2.3244885	1.400	201.1	45.6	9.60	0.5	0.61
cosmos-3-113	150.08089	2.3239765	1.257	190.7	160.1	9.27	0.5	0.45
cosmos-7-64	150.06325	2.4488557	1.320	228.8	212.9	9.51	0.1	−0.79
cosmos-13-80	150.12906	2.2307920	1.230	199.1	172.2	9.46	0.6	0.64
cosmos-28-132	150.10593	2.4162436	1.262	498.6	419.7	8.95	0.1	−0.04
goodss-6-124	53.199558	−27.863221	1.231	248.1	485.9	8.82	0.0	0.42
goodss-9-108	53.062504	−27.764822	1.232	193.0	197.7	9.13	0.1	0.31
goodss-21-24	53.198181	−27.878668	1.253	226.6	110.6	9.91	0.3	1.09
goodss-27-124	53.193836	−27.844275	1.237	344.4	738.1	8.93	0.0	0.27
goodss-30-67	53.099816	−27.730301	1.309	260.5	205.4	9.73	0.2	0.83

Notes.
[a] All physical properties are from our SED fitting.
[b] The [O III] line for this source is very noisy and the line fitting is uncertain. Therefore, we do not use the [O III] EW estimate for this source.

subtract the dark current and flat field the images. We use the dark image provided by the STScI as a reference to remove the primary dark component. This dark component does not account for the central glow, which rises with temperature. This excess dark component is later subtracted as explained in Section 2.4. The `Astrodrizzle` code was then used to combine the exposures and make the final drizzled image. Here, we weight the individual frames by their exposure time and we set the output pixel scale to 0.03″ and the pixfrac to 1. Because the SBC data have little sky background and are insensitive to cosmic rays, the sky subtraction and cosmic ray rejection steps have been turned off in running the `Astro-drizzle` code.

The images are drizzled and aligned to the Cosmic Assembly Near-infrared Deep Extragalactic Legacy Survey (CANDELS) F606W tiles. The relative astrometry between SBC and reference images is always better than 1–1.5 pixels (i.e., the rms of the best alignment fit). We note that the popular `Tweakreg` code for the HST image alignment fails due to lack of an adequate number of compact, bright sources. Therefore, we manually identify matching sources on the individual science and reference images, and then use the `PYRAF` `geomap` code to calculate the shift between the images.

We note that we could only align the images of seven sources. Of the remaining four (with IDs cosmos-7-64, cosmos-9-108, goodss-21-24, and goodss-30-67), no sources were detected in the individual SBC/F150LP images to be used for the alignment. Unless otherwise noted, we drop these four objects from the LyC analyses presented in this paper. Similar to the sample of seven sources that we will be discussing, we did not detect any LyC flux for these 4 objects in the F150LP images.

2.4. Dark Subtraction

As stated above, dark current is the dominant source of noise in these observations and a careful treatment of dark subtraction and its varying component is vital. Here, the total dark is a sum of the primary and excess dark components. We subtract these dark components separately in two stages. First, we subtract the primary calibration dark reference file,[9] which accounts for the low and stable dark current of

8.11 × 10^{-6} counts s^{-1} pix^{-1} when the instrument is <25°C. As explained in Section 2.3, the primary dark subtraction is part of the image processing done by the `CALACS` program.

Second, although each target is located in the least affected region on the detector, we check for additional dark current associated with the central glow. First from a visual inspection of different exposures in the image of each target, we define a border separating the corner with stable background from the central region with varying dark glow. We exclude those regions of the image where there are sources using a segmentation map from a `SExtractor` (Bertin & Arnouts 1996) run on F606W images. Using the F606W photometric aperture of each target (see Section 3), we then generate random apertures within the corner of each image and investigate the distribution of total flux within these regions. If the primary calibration dark image were adequate, we would expect each flux distribution to be centered at zero. However, these flux distributions are centered around nonzero values varying between [5.0, 11.0] × 10^{-6} counts s^{-1} pix^{-1}. This is evidence of an excess dark current with a value of ± 30% of the primary dark current (i.e., excess dark = (1 ± 0.3) × primary dark). Therefore, for each drizzled image, we subtract the median of the flux distribution of the random apertures within the corner. We use these improved drizzled images for our LyC analyses.

This excess dark current appears to increase with the detector temperature. We also investigate the possibility of a gradient in the excess dark and we find that it rises from corner edge toward the center by about 30%. However, this dark gradient does not affect our photometry because our sources are compact. Overall, these behaviors are consistent with those reported in Teplitz et al. (2006), Siana et al. (2007), and Avila (2017). However, our estimate of the excess dark current in the corner is much weaker than what these studies have reported for the central dark glow, thanks to our mitigation strategy.

3. Photometry

For the UV, optical and near-IR photometry, we use the public 3D-HST catalogs of the COSMOS and GOODS-South fields (Brammer et al. 2012; Skelton et al. 2014). They assembled the catalogs using a combination of three Wide Field Camera 3 (WFC3; MacKenty et al. 2010) bands of F125W, F140W, and F160W for the detection and the point-spread

---

[9] We downloaded the reference file 04k1844aj$_{drk}$ from the HST Calibration Reference Data System.

Table 2
Summary of LyC Measurements

ID	U [AB]	f_{1500} [μJy]	$f_{\rm LyC}$[a] [μJy]	IGM Transmission ($\exp(-\tau)$)	$f_{\rm LyC}/f_{1500}$[b]	$f_{\rm esc,rel}$[c]	$f_{\rm esc,abs}$[d]	$f_{\rm esc,abs}$[e]
cosmos-1-111	23.68	1.23	<0.015	0.56	<0.023	<0.18	<0.08	<0.11
cosmos-3-69	23.73	1.16	<0.011	0.56	<0.019	<0.15	<0.04	<0.06
cosmos-3-113	24.11	0.83	<0.012	0.56	<0.027	<0.22	<0.06	<0.13
cosmos-13-80	23.95	0.96	<0.008	0.61	<0.015	<0.12	<0.03	<0.04
cosmos-28-132	24.20	0.76	<0.008	0.56	<0.020	<0.16	<0.07	<0.06
goodss-6-124	24.10	0.83	<0.007	0.61	<0.014	<0.11	<0.07	<0.08
goodss-27-124	24.16	0.78	<0.006	0.61	<0.012	<0.10	<0.06	<0.04
stacks	⋯	6.54	<0.033.	0.60	<0.009	<0.07	<0.06	⋯

Notes.
[a] The LyC fluxes are 3σ limits.
[b] This ratio is corrected for the IGM absorption.
[c] An intrinsic ratio of $L_{1500}/L_{\rm LyC} = 8$ is assumed.
[d] These values are derived from adding dust correction to the $f_{\rm esc,rel}$ values.
[e] These values are derived directly from an estimate of intrinsic LyC luminosity using the Hα luminosity.

function-matched HST images of each field. For each galaxy, we use ground-based U-band ($\lambda_{\rm rest} \sim 1600$ Å) from CFHT MegaCam or VLT VIMOS and HST/SBC F150LP images to compute the observed non-ionizing and ionizing UV (i.e., LyC) fluxes, respectively.

To define apertures for LyC measurements, we started with the SExtractor segmentation maps of the 3D-HST catalogs. However, these photometric apertures are much larger than the area where we expect a significant rest-frame far-UV flux from each galaxy. Therefore, we define new isophotal apertures using shorter wavelength filters, which probe the rest-frame near-UV and thus areas of ongoing star formation in galaxies. Ideally, we would use the U-band images as our detection band but they are low-resolution ground-based data and require degrading the SBC images. We therefore choose to run the SExtractor in dual image mode using the optical F606W image, which corresponds to rest-frame $\lambda \sim 2600$ Å, for detection. We note that this is the same SExtractor measurement that was referred to in Section 2.4. Because the F606W image is deep (i.e., with 5σ depth of 28.3 and 29.4 magnitudes for COSMOS and GOODS-South, respectively), the isophotes are large. Using a solution discussed in Siana et al. (2007), we find that if we shrink the isophotes to include 80% of the F606W total flux, the area decreases by a factor of 1.5–2.7. This increases our far-UV sensitivity by 0.2–0.5 mag.

We calculate the 3σ upper limits of the LyC fluxes in two ways:

1. As explained above, the dark current is the dominating component of noise in the SBC images. We estimate the total dark current from the sum of the primary dark and excess dark component (see Section 2.3) within the isophotal aperture of each target. The total noise is then calculated as $\sqrt{{\rm total\ dark} \times {\rm exposure\ time} \times {\rm area}_{\rm isophot}}$.
2. We first use the F606W isophotal segmentation map to exclude all objects from the SBC images. We then randomly move the isophotal aperture of each target within the image corner where it is located and measure the flux within the aperture. The final noise is then derived from the standard deviation of the distribution of random aperture fluxes.

Our estimates of the limits from these two measurements agree within 10%. Unless otherwise noted, we use the limits from the second technique as listed in Table 2.

Finally, we correct the photometry for Galactic extinction using the values of $A_V = 0.051$ and 0.021 mag for COSMOS and GOODS-South, respectively, as reported in Skelton et al. (2014). These Galactic dust extinction values are based on the recalibration by Schlafly & Finkbeiner (2011) of the Cosmic Background Explorer (COBE) Diffuse Infrared Background Experiment (DIRBE) and IRAS Sky Survey Atlas (ISSA) dust maps. Assuming a Cardelli extinction curve (Cardelli et al. 1989) with $R_V = 3.1$, we estimate the $A_{1600} = 0.13$ and 0.05 mag, respectively.

4. Results

4.1. Individual Galaxies

We do not detect any individual galaxy with a signal-to-noise ratio (S/N) > 3 in the SBC LyC images. Figure 3 shows postage stamp images of the SBC far-UV and F606W of each of the targets. The distribution of the S/N values calculated using the second technique is shown in Figure 4. The distribution of the S/N is centered around zero with a mean value of −0.07 and standard deviation of 0.9. We also search for LyC flux that may exist offset (up to 2.0″) from the UV continuum as discussed in Iwata et al. (2009) and Nestor et al. (2013).

4.2. Stack

We stack the far-UV F150LP cutout images to estimate an average escape fraction. To display the stacked image (see Figure 5), we do a simple addition of F150LP 3″ × 3″ cutouts, centered at the position of each source in the F606W image. As shown in Figure 5, we do not detect a signal in the stacked image. We note that because galaxies have various sizes and morphologies, in the case of a simple addition, some galaxies will add noise to areas where other galaxies have flux. Therefore, to measure the stacked flux, we perform an optimized stacking (see Siana et al. 2010) by only summing the pixels that were in the isophotal segmentation of individual galaxy photometry (see Section 3). We also measure the total noise in the stack by adding the noise (i.e., $\sqrt{{\rm dark} \ast {\rm exposure\ time}}$) in quadrature in the pixels of
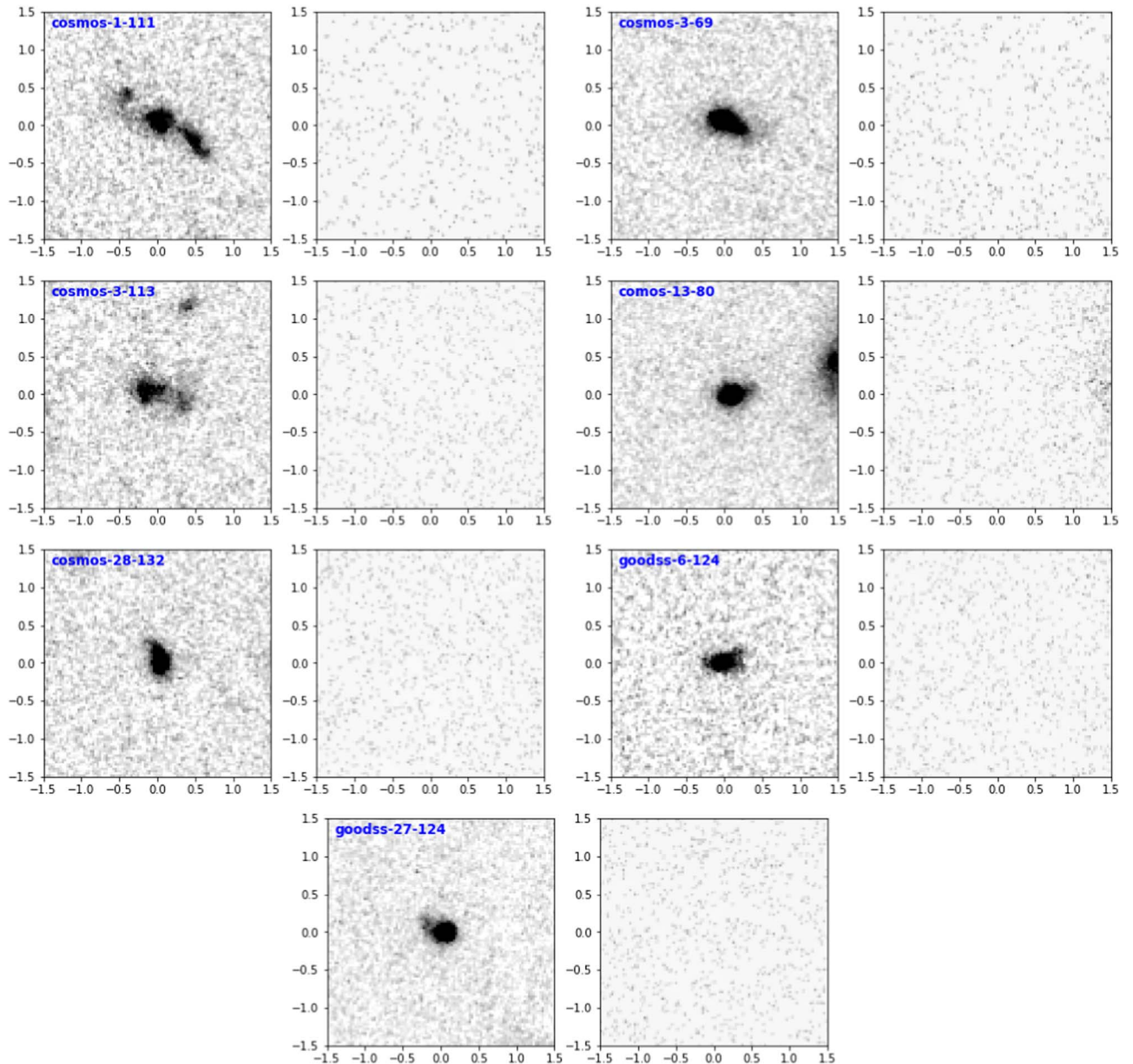
Figure 3. Postage stamp images of CANDELS F606W (left) and far-UV F150LP (right) of our targets. Each image is 3″ on each side. Most of these galaxies (except cosmos-1-111 and cosmos-3-113) display small and compact sizes. As can be seen in these images, none of these galaxies are detected in the F150LP images.

individual galaxies that were used in the optimal stacking. The total LyC flux in the stack image is $0.3 \times 10^{-31} \pm 1.1 \times 10^{-31}$ erg s^{-1} cm^{-2} Hz. The 3σ limit of the stacked flux is reported in Table 2.

4.3. Escape Fraction of Ionizing Photons

Lyman continuum radiation produced by young and hot stars is absorbed by neutral hydrogen inside galaxies and dust in the ISM, preventing that radiation from escaping the galaxy and reaching the IGM. There are two broadly used definitions for the LyC escape fraction in the literature.

First, the *absolute escape fraction*, $f_{\rm esc,abs}$, is simply the fraction of intrinsic LyC photons that escape into the IGM. This definition is convenient to use in theoretical and simulation studies where the true number of LyC photons produced is known from the SFR and initial mass function. However, this quantity is difficult to measure in observational studies because

it requires a measure of the intrinsic production rate of ionizing photons (i.e., LyC luminosity). The intrinsic LyC luminosity is usually estimated from nebular emission lines such as Hα or from the best-fit SED to the galaxy photometry. Both of these techniques need an understanding of the dust attenuation (i.e., dust extinction model) and thus they suffer from the associated uncertainties. For example, Steidel et al. (2018) show that changing the attenuation relation could change the estimated $f_{\rm esc,abs}$ by a factor of more than 3.

The second definition, first introduced by Steidel et al. (2001), is the *relative escape fraction*, $f_{\rm esc,rel}$, referring to the fraction of LyC photons that escape the galaxy relative to the fraction of escaping non-ionizing photons at 1500 Å. A benefit of this quantity is that it is independent of uncertainties in the estimation of dust correction. The $f_{\rm esc,rel}$ can be expressed as
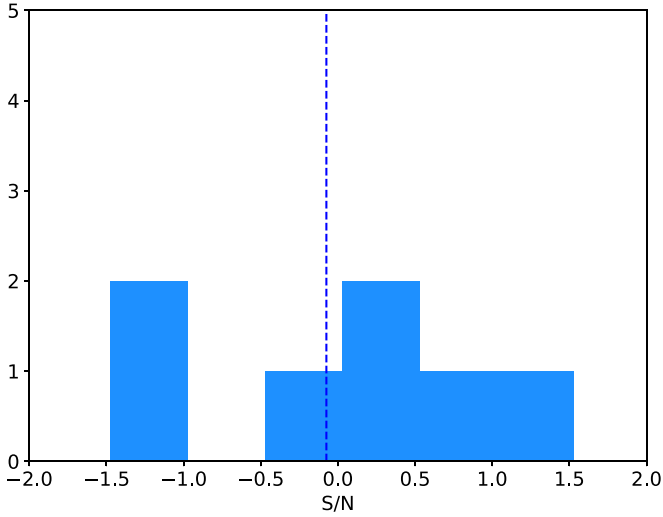
Figure 4. The distribution of the measured S/N of LyC fluxes for our sample of seven galaxies. There is no detection above S/N > 3. The distribution is nearly centered at zero with the dashed line indicating the arithmetic mean value at −0.07.
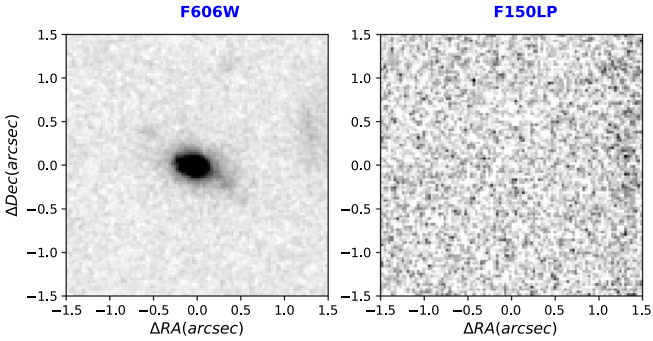

Figure 5. F606W (left) and far-UV F150LP (right) stacked images of our seven targets. We find no detection of LyC flux in the stacked image either.

below:

$$f_{\rm esc,rel} = \frac{f_{\rm LyC}^{\rm out}/L_{\rm LyC}^{\rm int}}{f_{1500}^{\rm out}/L_{1500}^{\rm int}} = \frac{(f_{\rm LyC}/f_{1500})^{\rm out}}{(L_{\rm LyC}/L_{1500})^{\rm int}}, \quad (1)$$

where the $f_{\rm LyC}^{\rm out}$ is the LyC flux density per unit frequency in the vicinity of galaxy right after escaping the ISM. Also, $f_{1500}^{\rm out}$ is the flux density per unit frequency measured at 1500 Å after passing through the galaxy ISM. These flux values are related to the observed fluxes as follows:

$$\left(\frac{f_{\rm LyC}}{f_{1500}}\right)^{\rm out} = \left(\frac{f_{\rm LyC}}{f_{1500}}\right)^{\rm obs} \times e^{\tau_{\rm IGM}(\rm LyC)}, \quad (2)$$

where $\tau_{\rm IGM}(\rm LyC)$ is the optical depth of LyC photons through the IGM along the LOS to that galaxy. We note that we measure the LyC flux at 700 Å, while it is usually measured at 900 Å in most studies (e.g., Steidel et al. 2001, 2018; Izotov et al. 2016a, 2016b; Marchi et al. 2017; Fletcher et al. 2019). Considering current observational facilities (i.e., SBC), we only have access to the ionizing flux at shorter wavelengths (700 Å) at z ∼ 1 (see also Siana et al. 2007, 2010).

As seen in Equations (1) and (2), to derive $f_{\rm esc,rel}$, we need to estimate the IGM absorption and the amplitude of the intrinsic

stellar Lyman break, $(L_{1500}/L_{\rm LyC})^{\rm int}$. Below, we summarize what we use for each of these quantities.

IGM: the IGM absorption ($e^{-\tau_{\rm IGM}}$) is computed from a Monte Carlo simulation described in detail in Siana et al. (2010) and Alavi et al. (2014). In summary, we create 300 different lines of sight through the IGM at different redshifts by selecting random hydrogen absorbing systems (i.e., Lyα forest, Lyman limit, and damped Lyα systems) from the density distribution associated with that redshift. We chose to run this simulation for 300 random lines of sight to accurately sample the column density and number density distributions of the intervening absorbers.

For this simulation, we adopt the number density and column density distributions of the intervening absorbers from the literature (Janknecht et al. 2006; Rao et al. 2006; Ribaudo et al. 2011; O'Meara et al. 2013) as explained in detail in Alavi et al. (2014). We then take the mean IGM absorption from 300 lines of sight for each redshift. The IGM absorption value that we used for each galaxy is listed in Table 2.

$(L_{1500}/L_{\rm LyC})^{\rm int}$: this intrinsic flux density ratio depends on the age, star formation history (SFH), metallicity, and IMF. Ideally, we would fit each individual SED with a stellar population model and derive the intrinsic flux decrement across the Lyman break. However as shown in Siana et al. (2010), the precise SFH is ambiguous and the best-fit SEDs from different SFHs give very different predictions of the intrinsic LyC flux. This is mainly because the portion of SED to which we are fitting the photometry is dominated by stars with ages >100 Myr, whereas the LyC flux comes from massive stars with ages <10 Myr. Relatedly, Rutkowski et al. (2016) argue that for a given SFH, the largest uncertainty in this intrinsic flux ratio is introduced by the ignorance of the stellar age and the IMF. They further show that this flux ratio can even be affected by stellar rotation and the choice of stellar template libraries. In addition, as discussed in Steidel et al. (2018), depending on the assumed age, metallicity, SFH, IMF, and the effect of binary evolution of massive stars, stellar population models predict a range of $0.15 < (L_{900}/L_{1500})^{\rm int} < 0.75$.

Here, we perform a simple analysis to quantify this ratio. We use BC03 (Bruzual & Charlot 2003) stellar population synthesis models with Chabrier IMF, constant SFH, and metallicity of $Z = 0.2\,Z_\odot$. We then derive the UV luminosity at two wavelengths: the ionizing continuum at 700 Å (i.e., the effective wavelength of the F150LP filter used in our SBC imaging) and non-ionizing UV at 1500 Å for a range of ages at [2 Myr, 5 Myr, 10 Myr, 30 Myr, 50 Myr, 100 Myr, 150 Myr, 200 Myr, 500 Myr, and 1 Gyr], as shown in Figure 6. At each age, following Inoue (2011), we derive the Hα fluxes and thus the Hα EWs as below:

$$L_{\rm H\beta} = 4.78 \times 10^{-13}\frac{1 - f_{\rm esc,abs}}{1 + 0.6f_{\rm esc,abs}}N_{\rm LyC}$$
$$L_{\rm H\alpha} = 2.78 \times L_{\rm H\beta}, \quad (3)$$

which results from the assumption of Case B recombination (Osterbrock & Ferland 2006). The factors in these equations are calculated by assuming a temperature $T = 10^4$ K and an electron density $n_e = 10^2$ cm^{-3}. $N_{\rm LyC}$ represents the stellar production rate of ionizing photons in units of s^{-1}. We note that we take into account the effect of nebular continuum in the UV flux ratio and Hα EW measurements. The Hα EW values are displayed on the x-axis in Figure 6. The galaxies in the
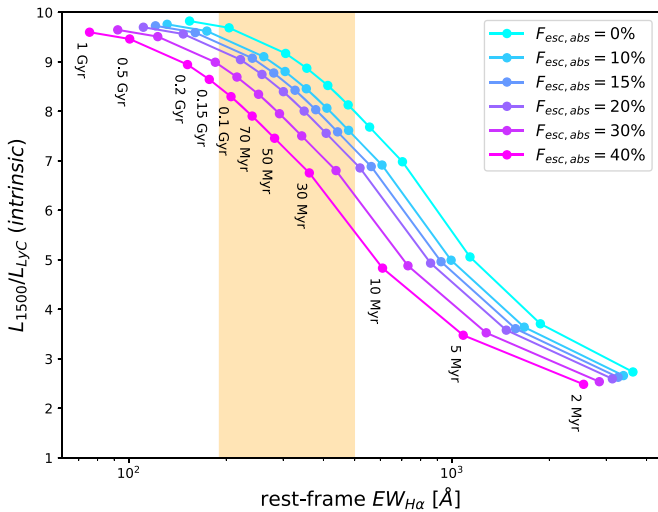
Figure 6. The $(L_{1500}/L_{\rm LyC})^{\rm int}$ intrinsic flux ratio as a function of rest-frame Hα EW using the BC03 models with $Z = 0.2\,Z_\odot$ and constant SFH. Each color specifies a different $f_{\rm esc,abs}$ value as listed in the figure. The Hα EW of galaxies in the observed sample is located in the shaded orange region.

sample have Hα EWs between 190 and 500 Å as shown in the orange area in Figure 6. We note that we are assuming a constant SFH here, while an instantaneous SFH would result in the same EW range at younger ages (Leitherer et al. 1999; Amorín et al. 2015). From this figure, we see that a $(L_{1500}/L_{\rm LyC})^{\rm int}$ ratio between 6 and 10 is required to reproduce the observed EW distribution with reasonable assumptions about the escape fraction. In what follows we use the average value of 8, which is consistent with the values used in some of the previous studies of starburst galaxies (i.e., similar to the galaxies in this study) at similar redshifts including Siana et al. (2007) and Rutkowski et al. (2016). We note that our estimate of the intrinsic luminosity density ratio is also in agreement with the value of 7 measured in Fletcher et al. (2019) for the LyC emitters with moderate emission-line EWs similar to our sample. However, as expected from Figure 6, our value is higher than the value estimated for the extreme LyC emitters with higher emission-line EWs including an intrinsic ratio of 1–5 assumed in Vanzella et al. (2016, 2018) and $\lesssim$6 inferred from the fitting to the intrinsic spectra in Izotov et al. (2018c).

Following Equations (1) and (2) and assuming an intrinsic ratio of 8, we estimate the $f_{\rm esc,rel}$ values as listed in Table 2. In addition, we also calculate the $f_{\rm esc,abs}$ values because several studies in the literature report their findings in terms of this quantity. To estimate this quantity, we use the relation of $f_{\rm esc,abs} = 10^{-0.4A_{1500}}f_{\rm esc,rel}$, as described in detail in Siana et al. (2007). Assuming a SMC curve, we derive the dust attenuation at 1500 Å, A_{1500}, using the $A_{\rm v}$ estimates (see Table 1) from our SED fitting. The $f_{\rm esc,abs}$ values are listed in Table 2.

As described above, our determination of the escape fraction uses the Hα EW to estimate the $(L_{1500}/L_{\rm LyC})^{\rm int}$ ratio with an assumed SFH. However, the assumptions made in this analysis could affect our estimate of the $(L_{1500}/L_{\rm LyC})^{\rm int}$ ratio, and thus the LyC escape fraction values. For example, Siana et al. (2007) showed that assuming an instantaneous SFH increases the $(L_{1500}/L_{\rm LyC})^{\rm int}$ ratio at a given age. We also note that accounting for the binary evolution of massive stars will decrease this ratio, as it enhances the late-time ionizing photon

production (Steidel et al. 2018; Fletcher et al. 2019). Another important uncertainty is the effect of older stellar populations in our interpretation of Hα EW. If there is an extremely young and strong burst of star formation on top of an older stellar population from previous bursts, then the Hα EW will not be as high as expected. This is because the older stellar populations dominate the rest-optical continuum and thus lower the Hα EW. To avoid this uncertainty, we can take the f_{1500} out of the equation and calculate the absolute LyC escape fraction directly from Hα luminosity. If we assume that LyC escape fraction is small, which is a reasonable assumption for our sample, we can then derive the total intrinsic LyC luminosity from the Hα luminosity assuming that all ionizing photons are absorbed and converted to Hα emission line via recombination. We note that Izotov et al. (2016b, 2018a) also adopted a similar technique to calculate the LyC escape fraction by relying on the fact that the Hβ emission-line intensity is proportional to the number of ionizing photons emitted per unit time. We use the above BC03 models and compute the conversion from Hα luminosity to LyC luminosity to be

$$L_{700}\ [\text{erg s}^{-1}\ \text{Hz}^{-1}] = 1.7 \times 10^{14} L_{\text{H}\alpha}\ [\text{erg s}^{-1}]. \qquad (4)$$

We calculate the Hα luminosity, $L_{\rm H\alpha}$, of our sample by correcting the observed Hα fluxes for dust attenuation assuming an SMC curve. We then use the above equation to derive the intrinsic LyC luminosity, L_{700}, for each galaxy in our sample. Finally, we calculate the $f_{\rm esc,abs}$ values using the ratio of the observed LyC flux limits corrected for the IGM absorption and the intrinsic L_{700} values from Equation (4). We report these new estimates of $f_{\rm esc,abs}$ in Table 2. These new values are in general agreement with our original $f_{\rm esc,abs}$ estimates.

As explained before in Section 2.2, we observed each galaxy in our sample with a different depth, which was calculated using the online HST Exposure Time Calculator to reach a 3σ limit for $f_{\rm esc,abs}$ of 5%. Our measured $f_{\rm esc,abs}$ values are consistent with our predicted limits.

5. Discussion

5.1. Comparison with Other Studies: Physical Properties (SED Fitting)

Given the low success rate of identifying LyC leakers at high redshifts, it is important to compare our sample with other samples and investigate the LyC escape fraction in the context of different physical properties of galaxies.

The photometry of our sample results from a combination of ground- and space-based imaging. This includes 44 and 40 broad photometric bands from the near-UV ($\lambda_{\rm rest} \sim 0.19\ \mu$m) to IRAC4 ($\lambda_{\rm rest} \sim 3.5\ \mu$m) in the COSMOS and GOODS-South fields, respectively. The 3D-HST catalogs provide the best SED fitting parameters for these galaxies, but they assume a metallicity of $1.0\,Z_\odot$. However, the low stellar masses (i.e., $\log(M^*/M_\odot) \sim 9$–10) of our sample suggest lower values of [0.2, 0.4] $Z_\odot$ for the metallicity (Wuyts et al. 2012). We perform our own SED fitting using the FAST code (Kriek et al. 2009) on BC03 stellar population models assuming a Chabrier IMF (Chabrier 2003). We assume an exponentially increasing SFH (i.e., SFH $\propto e^{t/\tau}$) with $7 < \log(\tau) < 10$, as argued in Reddy et al. (2012) for high-redshift galaxies. We allow the metallicity to change between two values [0.2, 0.4] $Z_\odot$. We also select an SMC extinction curve (Gordon et al. 2003) with a
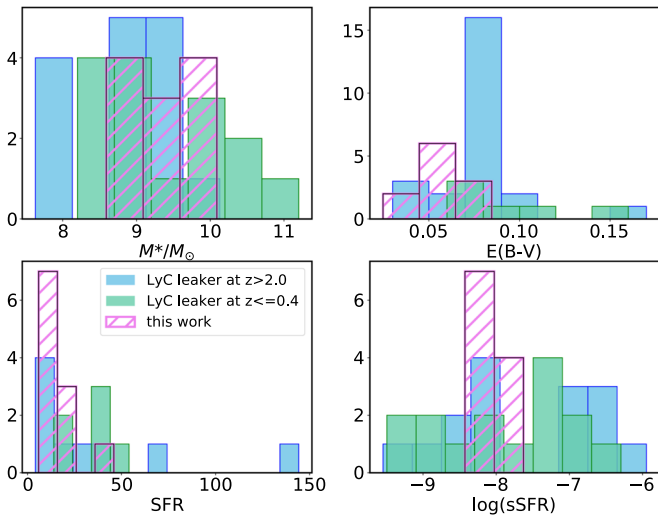
Figure 7. Histograms of the SED fit parameters of M_*, color excess $E(B-V)$, SFR, and sSFR. The confirmed LyC leakers from the literature are shown in blue and green for galaxies at $z > 2.0$ and $z < 0.4$, respectively. The parameter distributions of the galaxies in our sample are shown in pink-hashed histograms. These galaxies span a similar range of galaxy physical parameters as the other LyC emitters in the literature.

range of $0 < A_V < 4$. Some recent studies (Bouwens et al. 2016; Reddy et al. 2018) have demonstrated that $z = 1.5 - 2.5$ galaxies have an $IRX - \beta$ relation that is consistent with a steep extinction curve similar to SMC. In addition, we correct the broadband photometry for the contamination from nebular emission lines using the fluxes measured from the 3D-HST spectra. We note that the stellar mass estimates from our SED fitting are close to the 3D-HST stellar masses that we used for our initial sample selection. However, other parameters such as dust attenuation and SFR have significantly changed.

We compare the stellar masses (M_*), dust reddening parameterized as $E(B-V)$, SFR, and specific star formation rate (sSFR = SFR/M^*) of the galaxies in our sample with the quantities of confirmed LyC emitters from other studies. We divide the known LyC emitters in two groups of low $z < 0.4$ and high redshift $z > 2.0$ galaxies. We note that we scale the SFR and sSFR measurements to the Salpeter IMF (Salpeter 1955) for a fair comparison (i.e., multiplying our SFR estimates by a factor of 1.75). Caution must be taken when comparing SFR and color excess with other studies, because these parameters strongly depend on the dust attenuation models. For example, assuming a flat dust curve like Calzetti et al. (2000) would result in a larger value of $E(B-V)$. Therefore, for the comparisons of the $E(B-V)$ and SFR values, we only include the studies that use a similar extinction curve (i.e., SMC). In addition, to be consistent with our SFR estimate from the SED fitting, we only compare with the high-redshift studies that use an indicator sensitive to recent SFR (i.e., $\sim$100 Myr) in galaxies (Mostardi et al. 2015; Shapley et al. 2016; Vanzella et al. 2016, 2018; Bian et al. 2017; Naidu et al. 2017; Fletcher et al. 2019). However at low redshifts, we do not find recent SFR measurements corrected with the SMC curve in the literature. To compare with studies at $z < 0.4$, we use their SFR values obtained from extinction-corrected Hβ flux densities reported in Izotov et al. (2016a, 2016b, 2018a, 2018c). We note that SFRs from nebular emission lines trace the star formation activity on timescales of 10 Myr.

Figure 7 compares the distributions of four SED parameters of our non-detections (pink-hashed histogram) and the corresponding distributions of the other LyC leakers at low (green histogram) and high (blue histogram) redshifts. As seen in the upper-left panel of this figure, the stellar mass distribution of our non-detections overlaps with the stellar mass range covered by the LyC leakers at low and high redshifts. The mean value of our stellar mass distribution $\langle M^*/M_\odot \rangle = 9.5$ is halfway between the corresponding mean values of $\langle M^*/M_\odot \rangle = 10$ and $\langle M^*/M_\odot \rangle = 9.1$ for the LyC leakers at low and high redshifts, respectively.

We also examine the distribution of dust attenuation, $E(B-V)$, in the upper-right panel of Figure 7. The dust distribution of our non-detections overlaps with the lower end of the dust distributions for the LyC emitters.

Finally, as shown in the lower panels of Figure 7, both the SFR and sSFR histograms are consistent with the corresponding histograms of the LyC emitters. We should reemphasize that the SFR of low redshift LyC galaxies is derived from the Hβ emission line and thus it estimates the instantaneous SFR, while SFR estimates of our non-detections and high-redshift LyC galaxies are averaged over a timescale of $\sim$100 Myr.

In summary, although the confirmed LyC emitters cover a wide range of values for the physical properties discussed above, our measured values do fall within these observed distributions. Our observations demonstrate clearly that none of these parameters, alone, can guarantee a LyC-emitting galaxy.

In Figure 8, we show the observed ratio of $f_{\rm LyC}/f_{1500}$ corrected for the IGM absorption versus stellar mass (left) and UV absolute magnitude (right) measured at 1500 Å, M_{1500}. The quantity shown on the y-axis is the same as $(f_{\rm LyC}/f_{1500})^{\rm out}$ used in Equation (2). To ensure a fair comparison between these studies and to bring them to the same framework of IGM transmission estimates, we take the value of the observed ratio (or the 3σ limit) from each paper and correct for IGM absorption by adopting the correction factors at the relevant wavelength from our IGM simulations.

In these plots, we collected measurements of the LyC flux at different redshifts. The confirmed LyC detections are represented in two groups of high-redshift sources at $z > 2$ shown with colored circles (Mostardi et al. 2015; Shapley et al. 2016; Vanzella et al. 2016, 2018; Bian et al. 2017; Naidu et al. 2017; Steidel et al. 2018; Fletcher et al. 2019) and low-redshift sources at $z < 0.4$ shown with colored squares (Leitet et al. 2013; Borthakur et al. 2014; Izotov et al. 2016a, 2016b, 2018c). We also include the non-detection 3σ limits from studies of LyC candidates at $z > 1.0$ (Siana et al. 2007; Cowie et al. 2009; Bridge et al. 2010; Siana et al. 2010, 2015; Nestor et al. 2013; Amorín et al. 2014; Grazian et al. 2016; Guaita et al. 2016; Rutkowski et al. 2016; Marchi et al. 2017; Hernandez et al. 2018; Naidu et al. 2018; Smith et al. 2018). Our 3σ limits (black downward arrows) are lower than the ratio measured for the confirmed LyC leakers at higher and lower redshifts.

We also measured the LyC photon production efficiency ($\xi_{\rm ion}$) of our sample, as below:

$$\xi_{\rm ion} = \frac{1}{1.36 \times 10^{-12} [\rm erg]} \times \frac{L_{\rm H\alpha} [\rm erg\ s^{-1}]}{L_{\rm UV} [\rm erg\ s^{-1}\ Hz^{-1}]}, \quad (5)$$

where $L_{\rm H\alpha}$ and $L_{\rm UV}$ are the dust-corrected Hα and UV luminosity density at 1500 Å, respectively. The $\xi_{\rm ion}$ values of the galaxies in our sample change between
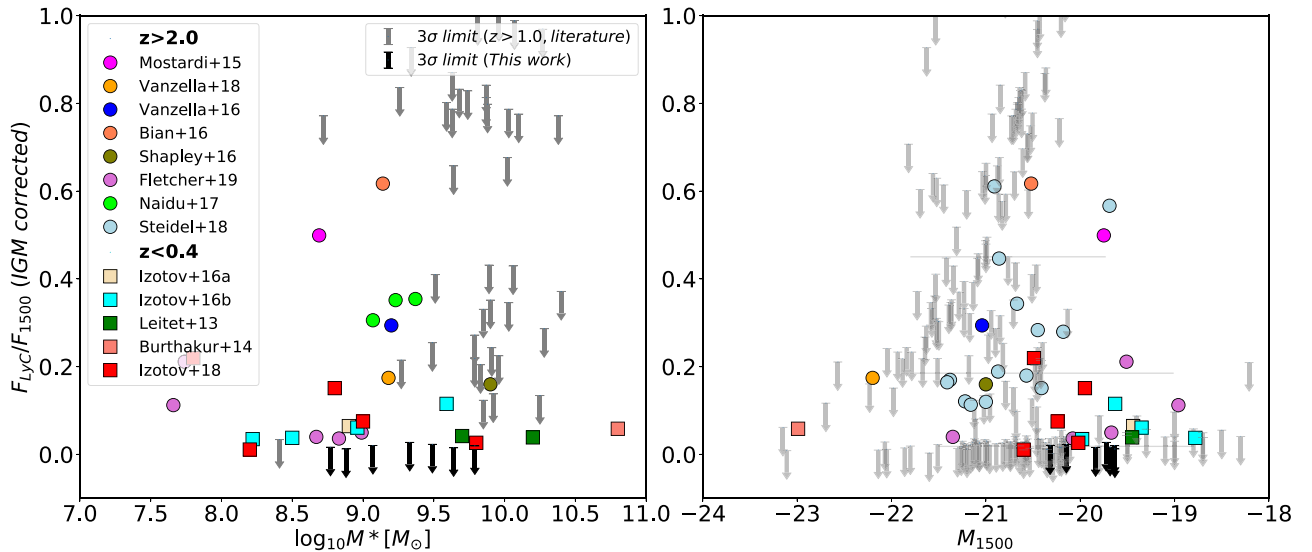
Figure 8. Left: the observed ratio of f_{LyC}/f_{1500} corrected for IGM absorption as a function of stellar mass. The LyC emitters from the literature are shown with colored circles and squares for galaxies at $z > 2$ and $z < 0.4$, respectively, as listed in the figure. Our 3σ non-detection limits are shown as black arrows. Right: the y-axis is similar to the left panel and the x-axis displays the UV absolute magnitude measured at 1500 Å. For both panels, the 3σ non-detections from the literature are from Siana et al. (2007), Cowie et al. (2009), Bridge et al. (2010), Siana et al. (2010), Nestor et al. (2013), Amorín et al. (2014), Siana et al. (2015), Grazian et al. (2016), Guaita et al. (2016), Rutkowski et al. (2016), Marchi et al. (2017), Hernandez et al. (2018), Naidu et al. (2018), and Smith et al. (2018). While the galaxies in our sample occupy the same range of M_* and M_{1500}, their flux ratio limits are lower than the ratio observed for LyC leakers.

$\log(\xi_{ion}) = 24.8 - 25.4$ [s^{-1}/erg s^{-1} Hz^{-1}] with a mean of 25.1. We note that only one galaxy in our sample has $\xi_{ion} = 24.8$, and the rest of the values are above 25.0. As discussed in Schaerer et al. (2016), the dust-corrected ionizing photon production rate of five low-redshift LyC emitters from (Izotov et al. 2016a, 2016b) vary between $\log(\xi_{ion}) = 25.1$–25.5. Therefore, the ionizing photon production efficiency of our sample is comparable with these LyC emitters. However, we should emphasize that the galaxies in our sample have lower LyC photon production efficiency than ion3 (Vanzella et al. 2018) as an extreme LyC emitter at $z = 4$ with $\xi_{ion} = 25.6$.

As an overall conclusion, the galaxies investigated in this study have similar physical properties to the LyC leakers, and thus likely the same intrinsic LyC production. Therefore, our low ratio of $(f_{LyC}/f_{1500})^{out}$ is likely related to the conditions in the ISM, such as high H I column density, and geometrical distribution of dust and neutral gas, which makes it difficult for photons to escape.

5.2. Comparison with Other Studies: Hα and [O III] EWs

Galaxies with intense rest-frame optical emission lines, EW (Hα and/or [OIII]) > 100 Å, are known as "Extreme Emission Line Galaxies" (EELG; see Atek et al. 2011). At the wavelengths of these nebular emission lines, the EW is indicative of the ratio of current SFR—thus numerous hot O-type stars producing ionizing LyC photons—to the integrated past SFR. Therefore, EELGs are undergoing a starburst episode with a significant population of new stars. Relatedly, Amorín et al. (2015) demonstrated that these galaxies are dominated by young (<10 Myr) star-forming regions. In a recent work, Reddy et al. (2018), using an extensive spectroscopic survey of star-forming galaxies at $z = 1.4$–3.8, show that high-EW galaxies, especially those with high [O III] EW, have both high ionization parameter and ionizing photon

production rate (i.e., ξ_{ion}). A more recent study by Tang et al. (2019) shows similar results. These characteristics have made EELGs ideal objects in which to search for escaping ionizing photons.

In addition, some studies (Henry et al. 2015; Yang et al. 2017) discovered that ∼70%–100% of green peas, EELGs with high [O III] EW at low-redshift, are strong Lyα emitters. Using Lyα radiative transfer simulations, Verhamme et al. (2015) argued that the detection of Lyα in emission from galaxies can be used to identify LyC emitters. Specifically, Lyα profiles can be indicative of LyC-leaking star clusters. They show a Lyα spectrum with either an asymmetric redshifted profile with small shift or nonzero Lα flux blueward of the systematic redshift can be an indicator of escaping LyC photons. In addition, some observational studies such as Steidel et al. (2018) and Fletcher et al. (2019) found high LyC escape fraction for Lyα emitters. This is another piece of evidence that EELGs are likely to be LyC emitters.

The incidence of galaxies with high EW of emission lines (either Hα or [O III] with rest-frame EW > 100 Å) in the currently available sample of LyC leakers at low redshifts (Izotov et al. 2016a, 2016b, 2018a, 2018c) and high redshifts (Vanzella et al. 2016, 2018; Naidu et al. 2017; Fletcher et al. 2019; Saha et al. 2020) suggests that high EW nebular emission lines may be a potential indirect tracer of a high escape fraction of ionizing photons. We investigate this by comparing the distribution of Hα (and [O III]) EWs of the confirmed LyC emitters and the non-detections including EELGs in this study.

Our sources are selected to have strong Hα emission lines and they cover the EW range between EW$_{Hα}$ = 190–500 Å. They also have intense [O III] emission lines with rest-frame EW$_{[OIII]}$ = 50–740 Å. As explained in detail in Section 4, we do not detect significant ionizing flux in either the individual galaxies or the stack. This is not the first time that observations of EELGs have not detected escaping LyC photons (e.g., Rutkowski et al. 2016; Naidu et al. 2018). Figure 9 compiles the LyC measurements including detections and non-
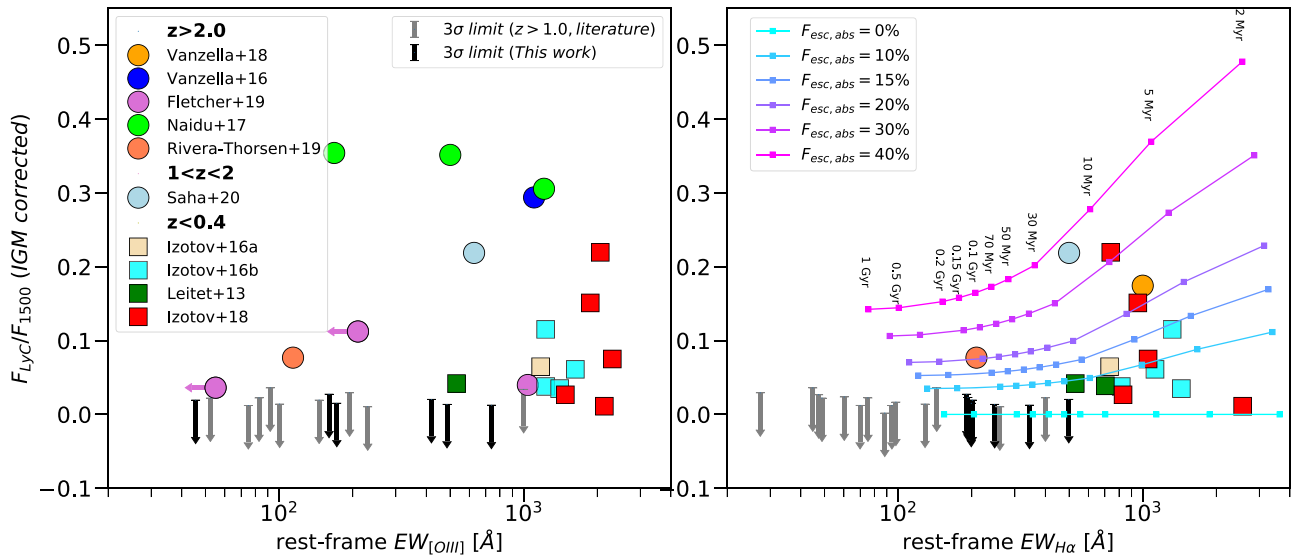
Figure 9. Left: the y-axis is similar to Figure 8 and the x-axis shows the rest-frame [O III] EW. Right: similar to the left panel with the x-axis values representing the Hα EW. For both panels, the 3σ non-detections from the literature are from Amorín et al. (2014), Rutkowski et al. (2016), Hernandez et al. (2018), and Naidu et al. (2018). The targets in the current work have a distribution of [O III] EW that is similar to the distribution observed in LyC leakers. This conclusion is less clear for the Hα EW, where the detections have nominally higher Hα EW values. One possibility is that the sample of LyC emitters with Hα EW measurement is somewhat incomplete due to lack of observations of the Hα line at $z > 2.5$, where most of the high-redshift LyC emitters are. The solid lines in the right panel are obtained from our simple BC03 models, which predict the value of $(f_{LyC}/f_{1500})^{out}$ at ages varying between 2 Myr and 1 Gyr for a range of LyC escape fraction assumptions.

detections, where an estimate of Hα and/or [O III] EW is available. It shows the IGM corrected f_{LyC}/f_{1500} as a function of [O III] EW in the left panel and Hα EW in the right panel.

[O III] EW: as can be seen in the left panel in Figure 9, galaxies in our sample (black arrows) span a wide range of rest-frame [O III] EW similar to the confirmed LyC leakers at lower and higher redshifts (Leitet et al. 2013; Naidu et al. 2017; Fletcher et al. 2019; Rivera-Thorsen et al. 2019; Saha et al. 2020). However, our sample does not cover the very extreme EW values (i.e., [O III] EW > 1000 Å) seen in some of the LyC emitters at low (Izotov et al. 2016b, 2018a, 2018c) and high redshift (Vanzella et al. 2016, 2020). This plot reconfirms the conclusion presented in previous studies (Izotov et al. 2017; Naidu et al. 2017; Fletcher et al. 2019) that high [O III] EW on its own is an insufficient diagnostic tool for the leakage of LyC photons.

Hα EW: in the right panel of Figure 9, we investigate the possibility of a correlation between detecting LyC photons and the EW of the Hα nebular emission line. Unfortunately, there are not many high-redshift LyC emitters for which a measurement of Hα EW is available. One galaxy at $z = 4$ from Vanzella et al. (2018),[10] one galaxy at $z = 2.4$ from Rivera-Thorsen et al. (2019), and a very recent finding at $z = 1.42$ from Saha et al. (2020) are the only high-redshift LyC emitters with Hα EW measurements. Therefore, any conclusion based on their small number should be used with caution. We note that among all of the high-redshift LyC leakers in the literature, more than 90% are at $z > 3$ where an estimate of the Hα EW is very challenging.

Our sample with moderate Hα EW at $EW_{Hα} = 190$–500 Å spans the same range of rest-frame Hα EW as some of the non-detections in the literature (Siana et al. 2010; Rutkowski et al. 2016; Hernandez et al. 2018; Naidu et al. 2018). The Hα EW

of a confirmed LyC emitter at $z = 2.37$ by Rivera-Thorsen et al. (2019) is also within this range. In contrast, the group of confirmed LyC emitters (filled squares and orange circle in the right panel of Figure 9) with extreme Hα EWs including several low-redshift sources at $z < 0.4$ and only one high-redshift galaxy (*ion*3 at $z = 4$ from Vanzella et al. 2018), looks to be separated from the non-detected sources at moderate Hα EWs. In what follows, we first suggest two scenarios that can explain the lack of LyC emitters seen at moderate Hα EWs. We then investigate whether Hα EW is an effective proxy for LyC emissivity.

5.2.1. Moderate Hα EW

As mentioned above, while searches for emerging LyC photons have yielded null results (except the study by Rivera-Thorsen et al. 2019) for galaxies with moderate Hα EWs, galaxies with extreme Hα EWs usually seem to be LyC emitters. This dichotomy (see the right panel of Figure 9) could be due to small number statistics. However, if the dichotomy is real, it could suggest that sources with moderate intensity Hα emission have a lower LyC escape fraction than that of the sources with extreme Hα EW. Below, we discuss these two scenarios.

First Scenario: we show that a moderate Hα EW does not necessary imply a null LyC emissivity, and thus the dichotomy seen in Figure 9 might be due to small number statistics. As pointed out before, the number of confirmed high-redshift LyC emitters with Hα EW measurements available is only two compared to the eight high-redshift LyC emitters with [O III] EW measurements discussed above. Here, we perform a validation experiment to predict the Hα EWs of those LyC emitters without Hα line measurements and to investigate if any of them are likely to have moderate Hα EW.

We select 3D-HST galaxies at $1.3 < z < 1.5$, where both Hα and [O III] emission lines are available. We remeasure the EW values of these two lines, because the 3D-HST catalogs

---

[10] It should be noted that the EW measurement for this redshift is not from spectroscopic data. Using its broadband photometry and a clear excess in the 3.6 μm flux, they estimate a rest-frame Hα EW of 1000 Å.
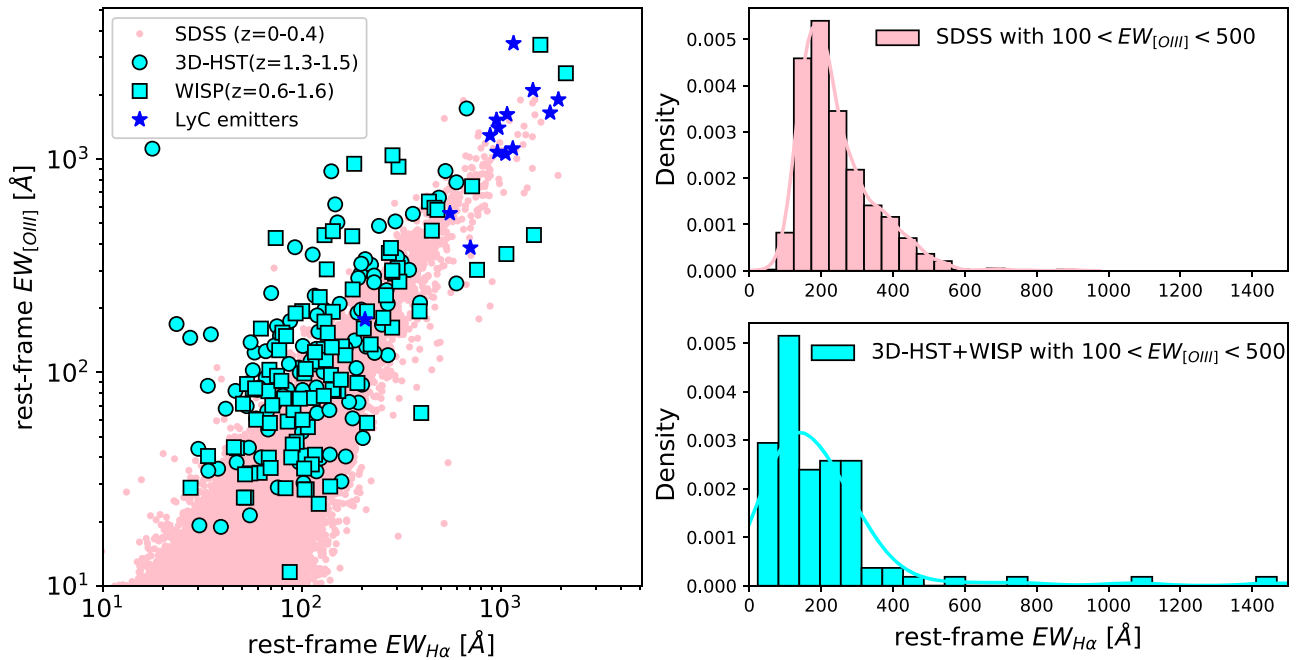
Figure 10. Left: this plot compares the rest-frame Hα and [O III] EW values of galaxies at $1.3 < z < 1.5$ in the 3D-HST survey. The correlation seen between these two quantities allows us to predict the Hα EW of the medium-intensity [O III] emitters. Right (top): the distribution of Hα EW of SDSS galaxies with moderate [O III] EW of $100 < EW < 500$. Right (bottom): the distribution of Hα EW of 3D-HST+WISP galaxies with moderate [O III] EW of $100 < EW < 500$. Both histograms peak around medium values of Hα EWs and they do not cover extreme vales of $\sim >600\,\text{Å}$.

have been reported to overestimate the EWs when the continuum detected by the grism is faint (Naidu et al. 2017). In addition, we include galaxies from the WFC3 Infrared Spectroscopic Parallel Survey (WISP; Atek et al. 2010). The WISP survey obtained slitless near-IR grism spectroscopy of more than 200 independent fields in pure-parallel mode with WFC3. This survey observes both Hα and [O III] emission lines for galaxies at $0.6 < z < 1.6$. For comparison, we also include a sample of $\sim$100,000 local galaxies at $z < 0.4$ drawn from the Sloan Digital Sky Survey (SDSS; York et al. 2000) DR12 release (Alam et al. 2015).

As shown in the left panel of Figure 10, the Hα and [O III] EWs strongly correlate such that we do not expect extreme Hα EW (i.e., $>600\,\text{Å}$) for moderate-intensity [O III] lines (i.e., $100 < EW_{[O\,III]} < 500$). To further investigate this quantitatively, we plot the distribution of Hα EW values for a range of moderate [O III] EW values of $100 < EW_{[O\,III]} < 500$ for SDSS and 3D-HST+WISP galaxies in the upper-right and lower-right panels of Figure 10, respectively. As seen in these histograms, galaxies with moderate [O III] EW values are very likely to be moderate Hα emitters. Therefore, those LyC emitters with moderate [O III] EW values (e.g., purple and light green circles in the left panel of Figure 9) and no Hα line measurement, are presumably moderate Hα emitters as well.

We should note that the intensity ratio of [O III]/Hα and their EWs are strongly dependent on metallicity. This can be inferred from the metallicity dependency of [O III]/Hβ ratio discussed in Maiolino & Mannucci (2019) and references therein. The [O III]/Hα ratio decreases as metallicity decreases and thus sources with very high Hα and moderate [O III] EWs are expected at very low metallicities. Indeed, two most metal-poor low-redshift galaxies with $12 + \log(\text{O/H}) \sim 7.0$ reported in Izotov et al. (2018b, 2019), have extreme Hα EW, whereas they have moderate [O III] emission lines. However, this metal-

deficient galaxies are likely very rare at intermediate and low redshifts.

In addition, from a theoretical point of view, it is possible to obtain an extreme Hα EW for a given moderate-intensity [O III] line. This is because the [O III] emission line is sensitive to the presence of very young hot stars, but Hα is instead sensitive to the presence of somewhat less extreme photons (i.e., 13.6 eV). However, as can be seen in Figure 10, observational values from SDSS, 3D-HST, and WISP surveys do not show many of such examples, and thus they must be rare.

In addition, we overplot the LyC emitters (blue stars) from literature in the left panel of Figure 10. As illustrated in this figure, the currently known LyC emitters follow the mean relation between the [O III] and Hα EWs seen in the SDSS, 3D-HST and WISP galaxies. Therefore, it is likely that the absence of moderate Hα emitters is just a selection effect.

Finally, we would like to emphasize that this scenario and its conclusion are solely based on the prediction of Hα EW values, and a definitive answer requires direct measurement of Hα emission lines for the LyC emitters with moderate [O III] EWs.

Second Scenario: the lack of galaxies with high LyC emissivity at moderate Hα EWs may be indicative of a real relation. To further investigate this possibility, we use our simple models (as described in Section 4.3) to understand how the observed ratio of f_{LyC}/f_{1500} changes with Hα EW. We calculate the observed f_{LyC}/f_{1500} ratios in our models by applying a range of assumed escape fraction values, $f_{\text{esc,abs}} = [0\%, 10\%, 20\%, 30\%, 40\%]$, to the intrinsic f_{LyC}/f_{1500} ratios calculated in Section 4.3. To be consistent with the observed ratios of the real galaxies, we also add the effect of dust attenuation at LyC and 1500 Å wavelengths, using a median of the color excess values, $E(B - V)$, of all the LyC emitters in the literature. As illustrated in the right panel of Figure 9, the observed ratios are calculated at different ages,

ranging from 2 Myr to 1 Gyr, corresponding to different Hα EWs.

The lines seen in the right panel of Figure 9 are the results of variation of age and LyC escape fraction in the models. The age parameter is changing in the direction of the x-axis such that stellar populations are aging as we move along these lines toward lower Hα EWs. On the other hand, the LyC escape fraction parameter causes the spread in the direction of the y-axis. Based on our simple models, we can think of galaxies with moderate Hα EWs to be similar to galaxies with extreme Hα EWs but with older ages. Therefore, if we assume that the distribution of LyC escape fraction at moderate Hα EWs is the same as the distribution seen at extreme Hα EWs, then we would expect to detect some LyC emitters at lower Hα EWs. Because we do not detect any LyC emission at these moderate Hα EWs, we can conclude that the LyC escape fraction in older starbursts (i.e., with moderate Hα EWs) must be lower.

In conclusion from the two scenarios described above, whether the lack of LyC emitters at moderate Hα EWs is due to small number statistics (i.e., first scenario in which we could see both LyC emitters and non-detections) or having a lower LyC escape fraction (i.e., second scenario in which we mostly see non-detections), moderate Hα EW, alone, is not a promising indicator of lyC leakage.

5.2.2. Extreme Hα EW

With the currently available data (i.e., finding only LyC emitters and no non-detections at extreme Hα EWs), we can suggest that an extreme Hα emission (i.e., Hα EW ~ 600–1000 Å and beyond) is likely an effective tracer of LyC emissivity. We note that LyC emissivity is a net effect of intrinsic LyC luminosity and LyC escape fraction. As understood from the models in the right panel of Figure 9, galaxies with similar LyC escape fraction (i.e., each colored solid line) have higher LyC emissivity (i.e., relative to the non-ionizing UV) at more extreme Hα EWs. A galaxy with higher LyC emissivity does not necessary have a higher escape fraction, but it could be a result of its higher intrinsic LyC luminosity. This will also make that galaxy a lot more likely to be detected. As an example, an extreme Hα emitter, J1248 + 4259, with Hα EW of 2561 Å from Izotov et al. (2018a) (shown with a red square in the right panel of Figure 9) has a very small LyC escape fraction (i.e., ~2%) but high enough LyC emissivity, which allows for a detection.

Finally, we should emphasize that the above discussions ignore the effect of redshift evolution on the properties of LyC emitters. As seen in Figure 9, all of the low-redshift LyC emitters have extreme [O III] and Hα EWs (i.e., >600 Å), while the high-redshift LyC emitters cover a wider range of EW values. A deeper understanding of possible redshift evolution requires a larger sample of confirmed LyC emitters at various redshifts.

5.3. Understanding the Non-detections

Our SED fits show that the physical properties (stellar mass, SFR, and dust attenuation) of the galaxies in our sample are similar to those of the confirmed LyC emitters. However, the galaxies in our sample have lower Hα EWs than almost all of the LyC emitters with Hα line measurements in the literature (with the exception of a study by Rivera-Thorsen et al. 2019). A direct interpretation of our results is that the galaxies in our

sample are older and thus they are likely to have lower LyC escape fraction (see Section 5.2 and the right panel of Figure 9). This simple interpretation explains why we did not detect escaping LyC emission in this study.

The above interpretation simply explains our non-detections in comparison with the LyC emitters with measured Hα EWs as can be seen in Figure 9. However, we saw (see Section 5.2.1) that this plot is probably more complicated than it looks. To further understand our non-detections in the context of these possible complications, we discuss other scenarios below.

While LyC emitters with Hα line measurements have extreme Hα EWs, we showed that LyC emitters with moderate Hα EWs possibly exist as well (see Section 5.2.1). If we accept such a possibility, we need to understand why the galaxies in our sample, with Hα EWs similar to those possible LyC emitters, have low LyC emissivity.

Because the stellar populations, and thus the LyC photon production of the galaxies in our sample and those possible LyC emitters at moderate Hα EWs are the same, the non-detections in our sample must be a result of the LyC photons not being able to escape. To further understand this, we consider a scenario suggested by hydrodynamical simulations (Cen & Kimm 2015; Ma et al. 2015; Paardekooper et al. 2015), in which the ionizing photons escaping from galaxies into the IGM are highly anisotropic. Consequently, as also noted in Paardekooper et al. (2015), even if the galaxies in our sample have high *actual* escape fraction, there can be many sight lines through which no ionizing radiation escapes. Therefore, our results strongly depend on the orientation of the galaxies. This emphasizes the importance of including large samples in the observational studies.

We note that the direction dependency of LyC escape fraction seems to be more significant at lower Hα EWs than is at extreme Hα EWs. As seen in Figure 9, all LyC searches at extreme Hα EWs resulted in LyC detections and there are no non-detections at these extreme EWs, in contrast to what we would expect for an anisotropic distribution of escaping LyC emission. To better understand this conflict, we consider a "picket fence" model in which the neutral gas surrounding the ionizing sources is patchy. In this model where parts of the galaxy are covered with optically thick clouds, LyC photons escape from optically thin holes between the clouds. The distributions of these holes and their sizes likely depend on how strong the galactic feedback is. In an extreme starburst (i.e., extreme Hα EW), strong stellar feedback may effectively expel neutral gas and lower the covering fraction, thus allowing LyC photons to escape more easily in different directions. However in a less extreme condition (i.e., moderate/low Hα EW), the covering fraction is higher and weaker stellar feedback creates random optically thin channels in the ISM (Zackrisson et al. 2013). In this situation, we can detect the LyC photons only if they are emitted in the thin channels directed toward our LOS.

Future observations of the LyC escape fraction will require a large, representative sample of galaxies. To achieve this goal, effective selection techniques will be vital. As is also discussed in Rutkowski et al. (2016) and Fletcher et al. (2019), we are lacking very low-mass galaxies (i.e., $\log(M_*/M_\odot) < 9$), the so-called dwarf galaxies, in the LyC studies at high redshifts including this study at $z \sim 1$. As suggested in many theoretical studies and most simulations (e.g., Yajima et al. 2011; Wise

et al. 2014; Lewis et al. 2020; Ma et al. 2020), these low-mass galaxies likely have a high escape fraction of ionizing photons. For example, a recent work by Ma et al. (2020) predicts that LyC escape fraction increases with stellar mass up to $M^* \sim 10^8\,M_\odot$ and decreases at higher masses. Therefore, a likely path for future studies of LyC escape fraction at $z \sim 1$ is to observe very low-mass dwarf galaxies as promising candidates for escaping ionizing radiation.

6. Summary

We have obtained ACS/SBC far-UV imaging of 11 star-forming galaxies at $1.2 < z < 1.4$ to search for escaping LyC emission. We select our targets from the 3D-HST survey to have strong Hα emission lines with EW > 190 Å and low stellar masses with $\log(M_*/M_\odot) < 10$. These criteria identify sources that are undergoing a starburst episode with a significant population of new stars and thus they are ideal to search for escaping ionizing photons. Our findings are as follows.

1. After careful data reduction and subtraction of the dark current as the dominant source of noise, we do not detect (i.e., S/N > 3) any escaping LyC radiation from the individual targets or in the stack.

2. We run a Monte Carlo simulation (Siana et al. 2010; Alavi et al. 2014) to compute the IGM absorption. This simulation properly accounts for varying opacity of the IGM along different lines of sight. Applying these IGM corrections, we calculate 3σ limits of $f_{\rm LyC}/f_{1500}$ <[0.014 − 0.027] and <0.009 for the individual galaxies and stack, respectively. Assuming an intrinsic ratio of $(L_{1500}/L_{\rm LyC})^{\rm int} = 8$, these limits translate to 3σ limits of $f_{\rm esc,rel} <$ [0.10, 0.22] and $f_{\rm esc,rel} < 0.07$ for the individual galaxies and stack, respectively.

3. We fit stellar population models to the multiband photometry of our sample covering from rest-frame UV to near-IR to estimate the physical parameters. The galaxies in our sample exhibit similar ranges of stellar mass, SFR, and dust attenuation values as the confirmed LyC emitters in the literature. Our findings indicate that none of these galaxy parameters, alone, is a promising indicator of LyC leakage.

4. We compare the Hα and [O III] EW values of our sample and those of the confirmed LyC emitters in the literature. Our Hα and [O III] EW estimates are in the range of EW$_{\rm rest}$ $\sim$ [190–500] Å and [50–700] Å, respectively. Our sample does not cover extreme values (i.e., >600 Å) seen in some of the LyC emitters in the literature (Izotov et al. 2016a, 2016b, 2018a, 2018c; Vanzella et al. 2016, 2018). For [O III] emission lines, we find that high [O III] EW values do not guarantee the detection of LyC flux. This conclusion is consistent with the findings from previous studies (Izotov et al. 2017; Naidu et al. 2017; Fletcher et al. 2019). For the Hα emission line, we demonstrate that a moderate EW (i.e., <600 Å) is not a promising indicator of leaking LyC photons. However, considering current evidence, it is likely that extreme Hα emission (i.e., ~600–1000 Å and beyond) is an effective indicator of higher LyC emissivity.

Future observations of LyC emission may have to combine various indirect selection techniques (i.e., profile of Lyα line, UV spectral slope, ultra-faint dwarf galaxies with very low stellar mass) to better identify LyC emitters at of $z \sim 1$.

ORCID iDs

Anahita Alavi ● https://orcid.org/0000-0002-8630-6435
Harry I. Teplitz ● https://orcid.org/0000-0002-7064-5424
Brian Siana ● https://orcid.org/0000-0002-4935-9511
Claudia Scarlata ● https://orcid.org/0000-0002-9136-8876
Michael Rutkowski ● https://orcid.org/0000-0001-7016-5220
Vihang Mehta ● https://orcid.org/0000-0001-7166-6035
Alaina Henry ● https://orcid.org/0000-0002-6586-4446
Y. Sophia Dai
(戴昱) ● https://orcid.org/0000-0002-7928-416X
Francesco Haardt ● https://orcid.org/0000-0003-3291-3704
Micaela Bagley ● https://orcid.org/0000-0002-9921-9218

References

Alam, S., Albareti, F. D., Allende Prieto, C., et al. 2015, ApJS, 219, 12
Alavi, A., Siana, B., Richard, J., et al. 2014, ApJ, 780, 143
Alavi, A., Siana, B., Richard, J., et al. 2016, ApJ, 832, 56
Amorín, R., Grazian, A., Castellano, M., et al. 2014, ApJL, 788, L4
Amorín, R., Pérez-Montero, E., Contini, T., et al. 2015, A&A, 578, A105
Atek, H., Malkan, M., McCarthy, P., et al. 2010, ApJ, 723, 104
Atek, H., Richard, J., Kneib, J.-P., & Schaerer, D. 2018, MNRAS, 479, 5184
Atek, H., Siana, B., Scarlata, C., et al. 2011, ApJ, 743, 121
Avila, R. J. 2017, Updated Measurements of ACS/SBC Dark Rates, STScI Tech. Rep. ISR ACS 2017-04
Bertin, E., & Arnouts, S. 1996, A&AS, 117, 393
Bian, F., Fan, X., McGreer, I., Cai, Z., & Jiang, L. 2017, ApJL, 837, L12
Borthakur, S., Heckman, T. M., Leitherer, C., & Overzier, R. A. 2014, Sci, 346, 216
Boutsia, K., Grazian, A., Giallongo, E., et al. 2011, ApJ, 736, 41
Bouwens, R. J., Aravena, M., Decarli, R., et al. 2016, ApJ, 833, 72
Bouwens, R. J., Illingworth, G. D., Oesch, P. A., et al. 2015, ApJ, 811, 140
Bouwens, R. J., Oesch, P. A., Illingworth, G. D., Ellis, R. S., & Stefanon, M. 2017, ApJ, 843, 129
Brammer, G. B., van Dokkum, P. G., Franx, M., et al. 2012, ApJS, 200, 13
Bridge, C. R., Teplitz, H. I., Siana, B., et al. 2010, ApJ, 720, 465
Bruzual, G., & Charlot, S. 2003, MNRAS, 344, 1000
Calzetti, D., Armus, L., Bohlin, R. C., et al. 2000, ApJ, 533, 682
Cardamone, C., Schawinski, K., Sarzi, M., et al. 2009, MNRAS, 399, 1191
Cardelli, J. A., Clayton, G. C., & Mathis, J. S. 1989, ApJ, 345, 245
Cen, R., & Kimm, T. 2015, ApJL, 801, L25
Chabrier, G. 2003, PASP, 115, 763
Chisholm, J., Rigby, J. R., Bayliss, M., et al. 2019, ApJ, 882, 182
Cowie, L. L., Barger, A. J., & Trouille, L. 2009, ApJ, 692, 1476
Deharveng, J. M., Buat, V., Le Brun, V., et al. 2001, A&A, 375, 805
Emami, N., Siana, B., Alavi, A., et al. 2020, ApJ, 895, 116
Erben, T., Hildebrandt, H., Lerchster, M., et al. 2009, A&A, 493, 1197
Faisst, A. L. 2016, ApJ, 829, 99
Fan, X., Carilli, C. L., & Keating, B. 2006, ARA&A, 44, 415
Ferland, G. J., Korista, K. T., Verner, D. A., et al. 1998, PASP, 110, 761
Fletcher, T. J., Tang, M., Robertson, B. E., et al. 2019, ApJ, 878, 87
Ford, H. C., Bartko, F., Bely, P. Y., et al. 1998, Proc SPIE, 3356, 234

Giallongo, E., Grazian, A., Fiore, F., et al. 2015, A&A, 578, A83
Giallongo, E., Grazian, A., Fiore, F., et al. 2019, ApJ, 884, 19
Gordon, K. D., Clayton, G. C., Misselt, K. A., Landolt, A. U., & Wolff, M. J. 2003, ApJ, 594, 279
Grazian, A., Giallongo, E., Gerbasi, R., et al. 2016, A&A, 585, A48
Grimes, J. P., Heckman, T., Aloisi, A., et al. 2009, ApJS, 181, 272
Guaita, L., Pentericci, L., Grazian, A., et al. 2016, A&A, 587, A133
Henry, A., Scarlata, C., Martin, C. L., & Erb, D. 2015, ApJ, 809, 19
Hernandez, S., Leitherer, C., Boquien, M., et al. 2018, MNRAS, 478, 1292
Hildebrandt, H., Pielorz, J., Erben, T., et al. 2009, A&A, 498, 725
Inoue, A. K. 2011, MNRAS, 415, 2920
Inoue, A. K., Shimizu, I., Iwata, I., & Tanaka, M. 2014, MNRAS, 442, 1805
Ishigaki, M., Kawamata, R., Ouchi, M., et al. 2018, ApJ, 854, 73
Iwata, I., Inoue, A. K., Matsuda, Y., et al. 2009, ApJ, 692, 1287
Izotov, Y. I., Guseva, N. G., Fricke, K. J., & Henkel, C. 2016a, MNRAS, 462, 4427
Izotov, Y. I., Schaerer, D., Thuan, T. X., et al. 2016b, MNRAS, 461, 3683
Izotov, Y. I., Schaerer, D., Worseck, G., et al. 2018a, MNRAS, 474, 4514
Izotov, Y. I., Schaerer, D., Worseck, G., et al. 2020, MNRAS, 491, 468
Izotov, Y. I., Thuan, T. X., & Guseva, N. G. 2017, MNRAS, 471, 548
Izotov, Y. I., Thuan, T. X., & Guseva, N. G. 2019, MNRAS, 483, 5491
Izotov, Y. I., Thuan, T. X., Guseva, N. G., & Liss, S. E. 2018b, MNRAS, 473, 1956
Izotov, Y. I., Worseck, G., Schaerer, D., et al. 2018c, MNRAS, 478, 4851
Janknecht, E., Reimers, D., Lopez, S., & Tytler, D. 2006, A&A, 458, 427
Jaskot, A. E., & Oey, M. S. 2013, ApJ, 766, 91
Kriek, M., van Dokkum, P. G., Labbé, I., et al. 2009, ApJ, 700, 221
Kulkarni, G., Worseck, G., & Hennawi, J. F. 2019, MNRAS, 488, 1035
Leitet, E., Bergvall, N., Hayes, M., Linné, S., & Zackrisson, E. 2013, A&A, 553, A106
Leitet, E., Bergvall, N., Piskunov, N., & Andersson, B. G. 2011, A&A, 532, A107
Leitherer, C., Ferguson, H. C., Heckman, T. M., & Lowenthal, J. D. 1995, ApJL, 454, L19
Leitherer, C., Hernandez, S., Lee, J. C., & Oey, M. S. 2016, ApJ, 823, 64
Leitherer, C., Schaerer, D., Goldader, J. D., et al. 1999, ApJS, 123, 3
Lewis, J. S. W., Ocvirk, P., Aubert, D., et al. 2020, MNRAS, 496, 4342
Livermore, R. C., Finkelstein, S. L., & Lotz, J. M. 2017, ApJ, 835, 113
Ma, X., Kasen, D., Hopkins, P. F., et al. 2015, MNRAS, 453, 960
Ma, X., Quataert, E., Wetzel, A., et al. 2020, arXiv:2003.05945
MacKenty, J. W., Kimble, R. A., O'Connell, R. W., & Townsend, J. A. 2010, Proc. SPIE, 7731, 77310Z
Maiolino, R., & Mannucci, F. 2019, A&ARv, 27, 3
Malkan, M., Webb, W., & Konopacky, Q. 2003, ApJ, 598, 878
Marchi, F., Pentericci, L., Guaita, L., et al. 2017, A&A, 601, A73
Mason, C. A., Fontana, A., Treu, T., et al. 2019, MNRAS, 485, 3947
Mason, C. A., Trenti, M., & Treu, T. 2015, ApJ, 813, 21
Masters, D., Capak, P., Salvato, M., et al. 2012, ApJ, 755, 169
Momcheva, I. G., Brammer, G. B., van Dokkum, P. G., et al. 2016, ApJS, 225, 27
Mostardi, R. E., Shapley, A. E., Steidel, C. C., et al. 2015, ApJ, 810, 107
Naidu, R. P., Forrest, B., Oesch, P. A., Tran, K.-V. H., & Holden, B. P. 2018, MNRAS, 478, 791
Naidu, R. P., Oesch, P. A., Reddy, N., et al. 2017, ApJ, 847, 12
Nakajima, K., & Ouchi, M. 2014, MNRAS, 442, 900
Nestor, D. B., Shapley, A. E., Kornei, K. A., Steidel, C. C., & Siana, B. 2013, ApJ, 765, 47
Nestor, D. B., Shapley, A. E., Steidel, C. C., & Siana, B. 2011, ApJ, 736, 18
Nonino, M., Dickinson, M., Rosati, P., et al. 2009, ApJS, 183, 244
Oke, J. B., & Gunn, J. E. 1983, ApJ, 266, 713

O'Meara, J. M., Prochaska, J. X., Worseck, G., Chen, H.-W., & Madau, P. 2013, ApJ, 765, 137
Ono, Y., Ouchi, M., Harikane, Y., et al. 2018, PASJ, 70, S10
Osterbrock, D. E., & Ferland, G. J. 2006, Astrophysics of Gaseous Nebulae and Active Galactic Nuclei (Sausalito, CA: University Science Books)
Paardekooper, J.-P., Khochfar, S., & Dalla Vecchia, C. 2015, MNRAS, 451, 2544
Parsa, S., Dunlop, J. S., & McLure, R. J. 2018, MNRAS, 474, 2904
Pelló, R., Hudelot, P., Laporte, N., et al. 2018, A&A, 620, A51
Pentericci, L., Vanzella, E., Fontana, A., et al. 2014, ApJ, 793, 113
Planck Collaboration, Adam, R., Aghanim, N., et al. 2016, A&A, 596, A108
Rao, S. M., Turnshek, D. A., & Nestor, D. B. 2006, ApJ, 636, 610
Reddy, N. A., Oesch, P. A., Bouwens, R. J., et al. 2018, ApJ, 853, 56
Reddy, N. A., Pettini, M., Steidel, C. C., et al. 2012, ApJ, 754, 25
Ribaudo, J., Lehner, N., & Howk, J. C. 2011, ApJ, 736, 42
Rivera-Thorsen, T. E., Dahle, H., Chisholm, J., et al. 2019, Sci, 366, 738
Robertson, B. E., Ellis, R. S., Furlanetto, S. R., & Dunlop, J. S. 2015, ApJL, 802, L19
Robertson, B. E., Furlanetto, S. R., Schneider, E., et al. 2013, ApJ, 768, 71
Rutkowski, M. J., Scarlata, C., Haardt, F., et al. 2016, ApJ, 819, 81
Rutkowski, M. J., Scarlata, C., Henry, A., et al. 2017, ApJL, 841, L27
Saha, K., Tandon, S. N., Simmonds, C., et al. 2020, NatAs, doi:10.1038/s41550-020-1173-5
Salpeter, E. E. 1955, ApJ, 121, 161
Sanders, R. L., Shapley, A. E., Kriek, M., et al. 2015, ApJ, 799, 138
Schaerer, D., Izotov, Y. I., Verhamme, A., et al. 2016, A&A, 591, L8
Schlafly, E. F., & Finkbeiner, D. P. 2011, ApJ, 737, 103
Shapley, A. E., Steidel, C. C., Pettini, M., Adelberger, K. L., & Erb, D. K. 2006, ApJ, 651, 688
Shapley, A. E., Steidel, C. C., Strom, A. L., et al. 2016, ApJL, 826, L24
Siana, B., Polletta, M. d. C., Smith, H. E., et al. 2008, ApJ, 675, 49
Siana, B., Shapley, A. E., Kulas, K. R., et al. 2015, ApJ, 804, 17
Siana, B., Teplitz, H. I., Colbert, J., et al. 2007, ApJ, 668, 62
Siana, B., Teplitz, H. I., Ferguson, H. C., et al. 2010, ApJ, 723, 241
Skelton, R. E., Whitaker, K. E., Momcheva, I. G., et al. 2014, ApJS, 214, 24
Smith, B. M., Windhorst, R. A., Jansen, R. A., et al. 2018, ApJ, 853, 191
Stark, D. P., Ellis, R. S., Chiu, K., Ouchi, M., & Bunker, A. 2010, MNRAS, 408, 1628
Stasińska, G., Izotov, Y., Morisset, C., & Guseva, N. 2015, A&A, 576, A83
Steidel, C. C., Bogosavljević, M., Shapley, A. E., et al. 2018, ApJ, 869, 123
Steidel, C. C., Pettini, M., & Adelberger, K. L. 2001, ApJ, 546, 665
Steidel, C. C., Strom, A. L., Pettini, M., et al. 2016, ApJ, 826, 159
Tang, M., Stark, D. P., Chevallard, J., & Charlot, S. 2019, MNRAS, 489, 2572
Teplitz, H. I., Siana, B., Brown, T. M., et al. 2006, AJ, 132, 853
Vanzella, E., Caminha, G. B., Calura, F., et al. 2020, MNRAS, 491, 1093
Vanzella, E., de Barros, S., Vasei, K., et al. 2016, ApJ, 825, 41
Vanzella, E., Guo, Y., Giavalisco, M., et al. 2012, ApJ, 751, 70
Vanzella, E., Nonino, M., Cupani, G., et al. 2018, MNRAS, 476, L15
Vanzella, E., Siana, B., Cristiani, S., & Nonino, M. 2010, MNRAS, 404, 1672
Vasei, K., Siana, B., Shapley, A. E., et al. 2016, ApJ, 831, 38
Verhamme, A., Orlitová, I., Schaerer, D., & Hayes, M. 2015, A&A, 578, A7
Willott, C. J., Delfosse, X., Forveille, T., Delorme, P., & Gwyn, S. D. J. 2005, ApJ, 633, 630
Wise, J. H., Demchenko, V. G., Halicek, M. T., et al. 2014, MNRAS, 442, 2560
Wuyts, E., Rigby, J. R., Sharon, K., & Gladders, M. D. 2012, ApJ, 755, 73
Yajima, H., Choi, J.-H., & Nagamine, K. 2011, MNRAS, 412, 411
Yang, H., Malhotra, S., Gronke, M., et al. 2017, ApJ, 844, 171
York, D. G., Adelman, J., Anderson, J. E., Jr., et al. 2000, AJ, 120, 1579
Yue, B., Castellano, M., Ferrara, A., et al. 2018, ApJ, 868, 115
Zackrisson, E., Inoue, A. K., & Jensen, H. 2013, ApJ, 777, 39